



THE UNIVERSITY *of* EDINBURGH  
**School of Physics  
and Astronomy**

**Senior Honours Project**  
**The evolution of the Caustic Skeleton:  
Studying Non-Gaussianities in the 2D  
Cosmic Web**

Guilherme Garcia  
28 of March 2025

**Abstract**

This project presents the first study of the effects of non-gaussianities in the cosmic web using the Caustic Skeleton method. It provides an overview of how the Zel'dovich approximation can be used as an alternative to hydrodynamical N-Body simulations to study the cosmic web and how this reveals the dependence of the cosmic structure on the deformation tensor of the primordial density field. Simultaneously, it presents a summary of the properties of Gaussian Random fields and how these can be used to generate realizations of Non-Gaussian fields based on their Bispectrum. These are used to produce 2D realizations of Local, Equilateral and Orthogonal non-gaussian fields and their respective caustic structure. A preliminary analysis of the fields shows that different non-gaussianities produce meaningful changes in the caustic structure, warranting the need for further studies to implement this method in a full 3D simulation.

**Declaration**

I declare that this project and report is my own work.

Signature:

Date: 28/3/2025

**Supervisor:** Dr. Job Feldbrugge

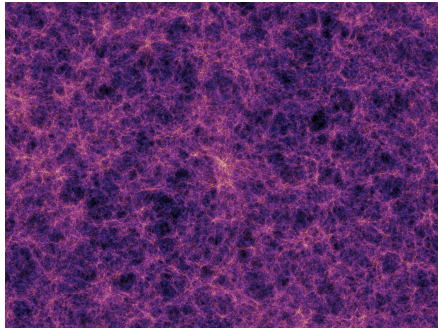
10 Weeks

# Contents

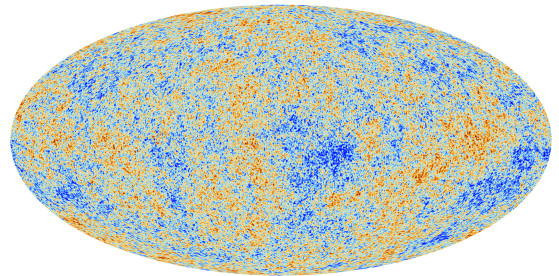
<b>1</b>	<b>Introduction</b>	<b>1</b>
<b>2</b>	<b>Cosmic Dynamics</b>	<b>2</b>
2.1	Zel'dovich Approximation . . . . .	4
<b>3</b>	<b>Random Fields</b>	<b>6</b>
3.1	Gaussian Random fields . . . . .	6
3.1.1	The Power Spectrum . . . . .	7
3.1.2	Constructing a Gaussian Random field . . . . .	8
3.1.3	Moments of a Gaussian Random field . . . . .	9
3.2	Non-Gaussian Random Fields . . . . .	10
3.2.1	Local Non-Gaussianities . . . . .	10
3.2.2	Field Reconstruction . . . . .	11
3.2.3	Equilateral and Orthogonal Non-Gaussianities . . . . .	14
<b>4</b>	<b>Caustic Theory</b>	<b>15</b>
4.1	Shell Crossing Conditions . . . . .	16
4.2	Caustic Conditions . . . . .	17
4.3	Computing Caustics . . . . .	19
<b>5</b>	<b>Caustics and non-Gaussianities</b>	<b>20</b>
<b>6</b>	<b>Discussion &amp; Conclusion</b>	<b>23</b>
<b>References</b>		<b>23</b>
<b>A</b>	<b>Wick's Theorem</b>	<b>27</b>
<b>B</b>	<b>Catastrophe Theory</b>	<b>28</b>
B.1	The Elementary Catastrophes in 2D . . . . .	29
B.2	Catastrophe theory in the Cosmic Web . . . . .	30
<b>C</b>	<b>Project Code</b>	<b>31</b>
<b>D</b>	<b>Further Non-Gaussian Realizations</b>	<b>38</b>

# 1 Introduction

When we look at our universe at its largest scale, we can observe a skeleton-like structure with high-density filaments separated by very low-density regions, as seen in figure 1(a). The cosmic skeleton originates from the initial small fluctuations in the density of the early universe, which are reflected in Cosmic Microwave Background (CMB), shown in figure 1(b) [1]. Measures of the CMB show that the temperature of the early universe only varies up to a part in  $10^5$  [1]. This primordial density field presents only very small non-gaussianities [2], while the cosmic skeleton we observe nowadays has a very non-gaussian nature.



(a) Artistic impression of the cosmic skeleton [3].



(b) The CMB as measured by the Planck Collaboration [4].

Figure 1: Illustrations of the nearly gaussian CMB and the highly non-gaussian cosmic skeleton of the current universe.

Understanding the nature of these primordial non-gaussianities can play a very important role in increasing our understanding of the universe, since it would allow us to distinguish between different theoretical models that predict different non-gaussian natures for the primordial density field [5–7]. While the primordial non-gaussianities can be directly measured from CMB surveys like WMAP(Wilkinson Microwave Anisotropy Probe) [8] or Planck [9], identifying the types of non-gaussianities purely from these surveys proves to be difficult due to the need to eliminate other non-gaussian contaminants. As such, it is relevant to look for alternative probes into this phenomena.

One alternative method is to study the effect of primordial non-gaussianities in large-scale structure formation. The success from large-scale structure formation models employing gaussian primordial densities, like the MillenniumTNG Project [10] or the Santa Cruz model for galaxy formation [11], indicate that while we can expect non-gaussianities to produce visible changes in the cosmic structure, these must be small. Several N-Body simulations have been used to simulate the large scale structure formation from initial non-gaussian fields like the Quijote-PNG [12, 13] or the PNG-UNITsims [14, 15]. However, the main goal of these simulations is to produce surveys of possible realizations of the caustic structure for the different cosmological parameters, including different non-gaussianities. This makes it harder to study the impact of parameter changes on specific geometric structures of the cosmic web, something that would be useful when looking for the small changes that are expected from the implementation of non-gaussianities. The Caustic Skeleton method [16] provides an analytical model to study the geometry of

the cosmic web, allowing for the study of its individual elements, like its filaments [17]. However, the studies employing this method so far approximate the primordial density field as gaussian.

This project aims to provide the first implementation for Local, Equilateral and Orthogonal non-gaussianities on 2D simulations of the cosmic web that allow the Caustic Skeleton method to study its underlying structure. Section 2 will start by presenting how cosmic evolution can be simulated, first through a hydrodynamical N-Body simulation model and then through the Zel'dovich approximation. Secondly, section 3 presents the main properties of Gaussian Random fields, how to construct a computational method to generate quick realizations of a gaussian primordial density field and how non-gaussian random fields can be generated by performing non-linear operations on an initial density field. Finally, section 4 presents how the Zel'dovich approximation can be used to study the underlying caustic structure of the cosmic web and how to apply this to the fields studied previously. Lastly, the implementation of all these concepts to provide a mathematical study of the effects of non-gaussianities in the 2D cosmic web is presented in section 5.

## 2 Cosmic Dynamics

To study cosmic evolution, it is necessary to start from the basics. Our universe is homogeneous, isotropic and is expanding in time. These characteristics can be described by the Friedman-Lemaître-Robertson-Walker (FLRW) metric [18]:

$$g_{uv} = \begin{pmatrix} -1 & 0 & 0 & 0 \\ 0 & a^2(t) & 0 & 0 \\ 0 & 0 & a^2(t) & 0 \\ 0 & 0 & 0 & a^2(t) \end{pmatrix}, \quad (1)$$

where  $a(t)$  is a time dependent scale factor, the Hubble expansion factor, that determines the relations between the coordinates through time, establishing a co-moving coordinate system. Using Einstein's field equations, that relate the metric with the constituents of the universe, it is possible to obtain a relationship between the Hubble expansion factor and the different cosmological parameters, the Friedman equation:

$$\dot{a} = aH_0\sqrt{\Omega_\Lambda + \Omega_m a^{-3} + (1 - (\Omega_\Lambda + \Omega_m))a^{-2}}, \quad (2)$$

where  $H_0$  is the Hubble parameter and  $\Omega_\Lambda, \Omega_M$  are the dark energy and matter density parameters, the relative weight of the dark energy and matter energy densities when compared with the critical density ( $\rho_c$ ), the total energy density for a flat universe.

$$\Omega_m = \frac{\rho_m}{\rho_c} \quad \Omega_\Lambda = \frac{\rho_\Lambda}{\rho_c} \quad \rho_c = \frac{3H_0^2}{8\pi G} \quad (3)$$

The study of large-scale structure formation focuses on the matter density evolution, and at this scale it is a reasonable assumption to consider dark matter as the dominating component (dark matter constitutes about 27% of the universe's energy density, but it constitutes about 85% of its mass constituents [19]). Similarly, gravity can also be considered the only relevant force at this scale. Using these assumptions, dark matter

can then be treated as a fluid under gravity [20], which means it will need to obey the hydrodynamical equations: the Poisson Equation (Equation 4), the Euler's Equation (Equation 5) and the continuity equation (Equation 6).

$$\nabla^2 \Phi = 4\pi G \rho. \quad (4)$$

$$\frac{\partial \mathbf{u}}{\partial t} + (\mathbf{u} \cdot \nabla) \mathbf{u} = -\nabla \Phi. \quad (5)$$

$$\frac{\partial \rho}{\partial t} + \nabla \cdot (\rho \mathbf{u}) = 0. \quad (6)$$

Equations 4, 5 and 6 show the hydrodynamical equations for a fluid under the effect of gravity.  $\Phi$  is the gravitational potential field,  $G$  is the gravitational constant,  $\rho$  is the mass density field and  $\mathbf{u}$  is the velocity field.

However, we are interested in studying a co-moving coordinated frame, as described by the metric in equation 1, as well as studying what effects the small perturbations have on the evolution of the density field. For this, we start by introducing a co-moving coordinate system,  $\mathbf{x} = \mathbf{r}a(t)$ , where  $a(t)$  is the Hubble expansion factor, relating the coordinates observed at a given time,  $\mathbf{x}$ , and the co-moving coordinates used to describe the system,  $\mathbf{r}$ . Similarly, we use perturbation theory, where  $\Phi = \Phi_0 + \phi$ ,  $\rho = \bar{\rho}(1 + \delta)$  and  $\bar{\delta} = 0$ , with  $\phi$  and  $\rho$  representing the gravitational and density potential perturbations. This returns a new form of the hydrodynamical equations [20, 21] :

$$\frac{1}{a^2} \nabla^2 \phi = 4\pi G \bar{\rho} \delta \quad (7)$$

$$\frac{\partial \mathbf{v}}{\partial t} + \frac{1}{a} (\mathbf{v} \cdot \nabla) \mathbf{v} + \frac{\dot{a}}{a} \mathbf{v} = -\frac{1}{a} \nabla \phi \quad (8)$$

$$\frac{\partial \delta}{\partial t} + \frac{1}{a} \nabla \cdot [(1 + \delta) \mathbf{v}] = 0 \quad (9)$$

with  $\mathbf{v} = a(t)\dot{\mathbf{r}}$  representing the co-moving velocity and  $\dot{a}$  the time derivative of Hubble's parameter. However Euler's equation, equation 8, can be further simplified by considering only terms linear in  $\mathbf{v}$ , since only small perturbations are considered:

$$\frac{\partial \mathbf{v}}{\partial t} + \frac{\dot{a}}{a} \mathbf{v} = -\frac{1}{a} \nabla \phi \Leftrightarrow a \frac{\partial \mathbf{v}}{\partial t} + \dot{a} \mathbf{v} = -\nabla \phi, \quad (10)$$

$$\partial_t(a\mathbf{v}) = -\nabla \phi. \quad (11)$$

Equation 11 shows the new form of the Euler's equation, defining the co-moving momentum as  $\mathbf{p} = a^2 \dot{\mathbf{r}} = a\mathbf{v}$ , it is clear that this can be seen as an analogous to Newton's second law.

Similarly, equation 7 can be further simplified by considering the definition of  $\Omega_m$  in Equation 3 and setting  $\bar{\rho} = \frac{\rho_m(t=0)}{a^3}$ , since the density in Poisson's equation is in co-moving coordinates and thus needs to be scaled as well:

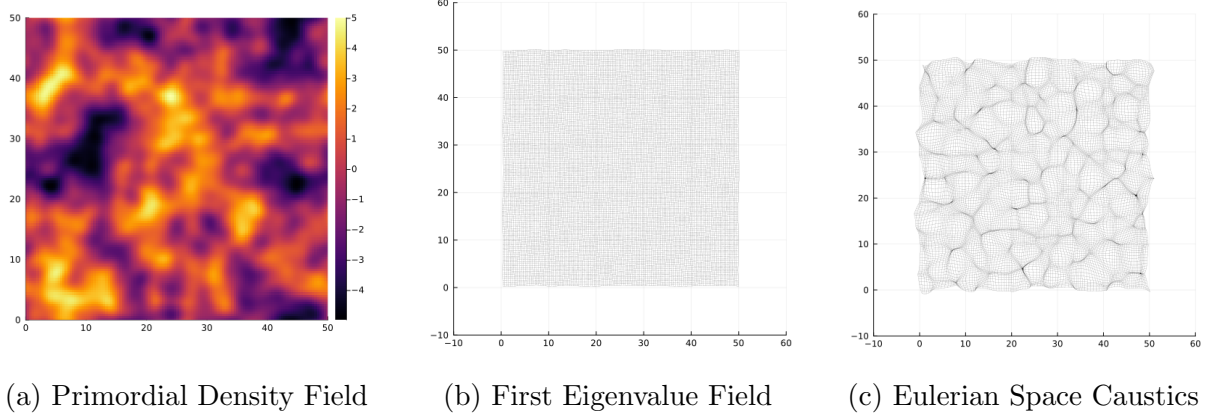


Figure 2: N-Body simulation of an initial particle field (2(b)), whose positions are determined by its initial(primordial) density field ((2(a))), which will also determine its later evolution (2(c)).

$$a\nabla^2\phi = \frac{3}{2}\Omega_m H_0^2\delta. \quad (12)$$

Using this hydrodynamical equations we can describe the evolution of a particle from the initial coordinate space,  $\mathbf{q}$ , at  $t = 0$  to a later time coordinate space  $\mathbf{x}$  :

$$\mathbf{x} = \mathbf{q} + \int \frac{\mathbf{v}}{a} dt. \quad (13)$$

The hydrodynamical equations thus provide a method to study the evolution of the mass density of the universe. The gravitational potential  $\phi$  is determined by the initial density field, helping to solve Poisson's Equation (Equation 12). Secondly, solving Euler's Equation (Equation 11) returns the velocity field, which can be used to find the new field position with Equation 13. Meanwhile, the continuity equation (Equation 9), ensures mass conservation throughout this process. Using this model makes it possible to develop a simulation that repeatedly solves these equations to study the evolution of the universe's large scale, using as only initial input the primordial density field (as it is shown in figure 2). In this project we use a particle mesh code [22] for a 2D implementation of the evolution of the cosmic structure, implemented by Job Feldbrugge, based on the code developed by Johan Hiding [23].

## 2.1 Zel'dovich Approximation

A more effective way to study the evolution of the density field, is by applying the Zel'dovich approximation (ZA). First proposed by Yakov B. Zel'dovich [24], this approximation assumes a linear behavior to explain the early stages of structure formation [25].

$$\mathbf{x}(\mathbf{q}, D_+(t)) = \mathbf{q} + D_+(t)\mathbf{s}(\mathbf{q}), \quad (14)$$

Equation 14 presents the Zel'dovich approximation describing the evolution of a mass element from an initial coordinate space, the Lagrangian space,  $\mathbf{q}$ , to a final coordinate space at a given time  $t$ , the Eulerian space,  $\mathbf{x}(t)$ . This only depends on the linear density

growth factor,  $D_+$  and the displacement field,  $\mathbf{s}(\mathbf{q})$ .

The growth factor is completely described by Eisntein's field equation [26] and thus depends only on the cosmological parameters, while  $\mathbf{s}(\mathbf{q})$ , the displacement field can be described as potential vector field [16, 27]:

$$\mathbf{s}(\mathbf{q}) = -\nabla_{\mathbf{q}}\psi(\mathbf{q}), \quad (15)$$

where  $\psi$  is the velocity potential [28], that can be described as:

$$\psi(\mathbf{q}) = \frac{2}{3\Omega_0 H_0^2} \phi_0(\mathbf{q}), \quad (16)$$

where  $\Omega_0$  refers to the current total energy density and  $\phi_0$  is the initial gravitational potential.

The deformation tensor ( $M$ ) is defined as the gradient of the displacement field with respect to the Lagrangian coordinates ( $\mathbf{q}$ ), as shown in equation 17 [16].

$$M = \frac{\partial \mathbf{s}(\mathbf{q})}{\partial \mathbf{q}}. \quad (17)$$

Using this approximation, it is possible to calculate the mass density field at a given time. Mass conservations implies that all the mass at Eulerian space must be the same at Eulerian space:

$$\rho(\mathbf{x}, t) d\mathbf{x} = \bar{\rho}(t) d\mathbf{q}, \quad (18)$$

from this, it is possible to obtain an equation for the density field:

$$\rho(\mathbf{x}, t) = \bar{\rho}(t) \left| \frac{\partial \mathbf{x}}{\partial \mathbf{q}} \right|^{-1}, \quad (19)$$

where  $\left| \frac{\partial \mathbf{x}}{\partial \mathbf{q}} \right|$  is the Jacobian determinant of the map between the Eulerian and Lagrangian spaces. This can be modified into a friendlier form by using Equation 14:

$$\rho(\mathbf{x}, t) = \frac{\bar{\rho}(t)}{|(1 + D_+(t)\alpha)(1 + D_+(t)\beta)|}. \quad (20)$$

Equation 20 shows how, in the Zel'dovich approximation, the density field at a given time  $t$  can be described using only the eigenvalues of the deformation tensor,  $\alpha$  and  $\beta$ , where  $\beta \leq \alpha$ . The deformation tensor only depends on the initial density field and the cosmological parameters.

One aspect to note when applying the Zel'dovich approximation, is that formally it should only work for  $|\alpha D_+| \ll 1$  and  $|\beta D_+| \ll 1$ , however, it has been confirmed that this approximation remains good until the beginning of the non-linear stage,  $D_+\alpha \approx 1$  [25]. It is this ability to extend this approximation beyond the theoretically expected limit that provides an opportunity to better study the geometry of the large scale structure as it forms the cosmic web. When  $D_+\alpha \approx 1$  or  $D_+\beta \approx 1$ , the density will become indeterminate, meaning it will form points of momentarily infinite density, called caustics.

The cosmic web can be characterized by its different multi-stream regions, these corresponds to dividing the Eulerian space according to the number of points of the Lagrangian space that map to the same point in the Eulerian space. For example, a 3-stream region will correspond to a region in Eulerian space in which every single point maps to three different points in the Lagrangian space. The higher the number of streams in a region, the higher its density, since we start by assuming that every point in Lagrangian space has the same mass. Caustics can be associated to crossings between multi-stream regions and will correspond to different structures that we can see in our universe [27]. This is exactly what defines the Caustic Skeleton method, using the caustics in the cosmic web to identify and study its structures. However to identify these different geometries we must first study the primordial density field ( $\phi_0$ ), that determines the later properties of the cosmic web, as well as finding a method to classify the caustics associated to each structure.

## 3 Random Fields

To study the properties of the quasi-gaussian density fields that originate the cosmic web, it is necessary to understand how to computationally simulate fields with the same properties. In order to do this, it is necessary to first study the properties of Gaussian Random fields in order to understand how these can be simulated and then used to generate their non-gaussian counterparts.

### 3.1 Gaussian Random fields

In general, a random field can be seen as a set of random variables,  $\theta$ , one for each point in space that can be characterized by a probability functional  $P[\theta]$  [1]. A given field  $\theta$ , is thus just one of the possible realizations of a field that obeys the probability functional.

Equation 21 shows the equation for a d-dimensions normal distribution, with  $\mu$  being the mean of the field and  $\sum$  the covariance matrix (a generalization of the standard deviation) and  $|\sum|$  represents its modulus.

$$G(\mathbf{x}) = \frac{1}{\sqrt{(2\pi)^d |\sum|}} \exp \left( -\frac{1}{2} (\mathbf{x} - \mu)^T \sum^{-1} (\mathbf{x} - \mu) \right). \quad (21)$$

A Gaussian random field is the generalization to the function space of this distribution [27]. This project, will focus solely on 2D fields  $f: \mathbb{R}^2 \rightarrow \mathbb{R}$ , whose probability distribution functional is described as:

$$P[f] = \frac{1}{|K|} \exp \left( -\frac{1}{2} \iint [f(\mathbf{q}_1) - \bar{f}(\mathbf{q}_1)] K(\mathbf{q}_1, \mathbf{q}_2) [f(\mathbf{q}_2) - \bar{f}(\mathbf{q}_2)] d\mathbf{q}_1 d\mathbf{q}_2 \right), \quad (22)$$

where  $\bar{f}(\mathbf{q})$  is the mean field and  $K$  is the kernel. This can be seen as an euclidean path integral,  $P[f] = \exp(-S[f])$ , where the exponent  $S$  can be seen as the classical action. Using this analogy with field theory, it is then trivial to deduce an equation for an expectation value of a given functional:

$$\langle Q[f] \rangle = \frac{1}{|K|} \int Q[f] e^{-S[f]} Df, \quad (23)$$

where  $Df$  is the sum over all possible functions. Similarly, it can be proven that the expectation value of a Gaussian random field is its mean field ( $\langle f(\mathbf{q}) \rangle = \bar{f}(\mathbf{q})$ ) [28].

To describe the properties of this field, it is necessary to define the 2 point correlation function ( $\varepsilon$ ), the relation between any two points of the field:

$$\begin{aligned} \varepsilon(\mathbf{q}_1, \mathbf{q}_2) &= \langle (f(\mathbf{q}_1) - \bar{f}(\mathbf{q}_1))(f(\mathbf{q}_2) - \bar{f}(\mathbf{q}_2)) \rangle \\ &= \int Df (f(\mathbf{q}_1) - \bar{f}(\mathbf{q}_1))(f(\mathbf{q}_2) - \bar{f}(\mathbf{q}_2)) e^{-S[f]}, \end{aligned} \quad (24)$$

this can be proven to be the inverse of the kernel:

$$\int K(\mathbf{q}_1, \mathbf{q}) \varepsilon(\mathbf{q}, \mathbf{q}_2) d\mathbf{q} = \delta_D^{(2)}(\mathbf{q}_1 - \mathbf{q}_2). \quad (25)$$

These fields can be further simplified by considering the environment they are describing. The goal of implementing a Gaussian Random field is to have a possible realization of the initial density field. This means we can assume the Cosmological principle, that our universe is homogeneous and isotropic [18, 28]. This means that the fields constructed must have a constant mean (which can be set to zero for simplicity), and that the two-point correlation function depends only on the the distance between the two points and not their actual position,  $\varepsilon(\mathbf{q}_1, \mathbf{q}_2) \rightarrow \varepsilon(|\mathbf{q}_1 - \mathbf{q}_2|)$ .

### 3.1.1 The Power Spectrum

Working with the Fourier transform of a random field ( $\tilde{f}$ ) will help better understand its statistical properties. For this, it is necessary to first define what we mean by the Fourier transform:

$$\tilde{f}(\mathbf{k}) = \text{FT}[f] = \int f(\mathbf{q}) e^{i\mathbf{k} \cdot \mathbf{q}} d\mathbf{q} \quad f(\mathbf{q}) = \text{FT}^{-1}[\tilde{f}] = \int \tilde{f}(\mathbf{k}) e^{-i\mathbf{k} \cdot \mathbf{q}} \frac{d\mathbf{k}}{(2\pi)^2}. \quad (26)$$

The Power Spectrum of a random field is defined as the Fourier transform of its two point correlation function:

$$P(\mathbf{k}) = \int \varepsilon(\mathbf{q}) e^{i\mathbf{k} \cdot \mathbf{q}} d\mathbf{q}. \quad (27)$$

Using this definition it is possible to obtain the Fourier space form of equation 25:

$$\int \tilde{K}(\mathbf{k}) P(\mathbf{k}) e^{i\mathbf{k} \cdot (\mathbf{q}_1 - \mathbf{q}_2)} \frac{d\mathbf{k}}{(2\pi)^2} = \delta_D^{(2)}(\mathbf{q}_1 - \mathbf{q}_2), \quad (28)$$

where  $\tilde{K}$  is the Fourier transform of the kernel, implying that  $\tilde{K}(\mathbf{k}) = \frac{1}{P(\mathbf{k})}$ .

The goal of using the Fourier formalism is to find a simplification of  $P[f]$  shown in equation 30 in order to easily construct simulations of the initial (primordial) density

field. To do this we use the double convolution theorem to simplify  $S[f]$ .

$$S[f] = \frac{1}{2} \iint f(\mathbf{q}_1) K(|\mathbf{q}_1 - \mathbf{q}_2|) f(\mathbf{q}_2) d\mathbf{q}_1 d\mathbf{q}_2 = \int |\tilde{f}(\mathbf{k})|^2 \tilde{K}(\mathbf{k}) \frac{d\mathbf{k}}{(2\pi)^2}. \quad (29)$$

Using the fact that the field being studied is homogeneous and isotropic, the power spectrum can be simplified as  $P(\mathbf{k}) = P(|\mathbf{k}|)$ . Furthermore, considering we are dealing with a real gaussian random field, its Fourier modes will need to obey the reality condition,  $\tilde{f}(\mathbf{k}) = \tilde{f}^*(-\mathbf{k})$ . The Fourier modes will fully describe the field in real space, thus their probability density functional can be deduced to be:

$$P[\tilde{f}] \propto \exp \left( -\frac{1}{2} \int \frac{|\tilde{f}(\mathbf{k})|^2}{P(\mathbf{k})} \frac{d\mathbf{k}}{(2\pi)^2} \right). \quad (30)$$

From this, the variance in Fourier space can be determined as:

$$\begin{aligned} \langle \tilde{f}(\mathbf{k}_1) \tilde{f}^*(\mathbf{k}_2) \rangle &= \iint e^{i(\mathbf{k}_1 \cdot \mathbf{q}_1 - \mathbf{k}_2 \cdot \mathbf{q}_2)} \langle f(\mathbf{q}_1) f(\mathbf{q}_2) \rangle d\mathbf{q}_1 d\mathbf{q}_2 \\ &= (2\pi)^2 \delta_D^{(2)}(\mathbf{k}_1 - \mathbf{k}_2) P(\mathbf{k}_1). \end{aligned} \quad (31)$$

### 3.1.2 Constructing a Gaussian Random field

The characteristics of a Gaussian random field make it possible to construct an algorithm to simulate them by using Fast Fourier Transform (FFT) methods.

Firstly, it was proven that the Fourier modes of a GRF are in themselves normal and independent of each other, it is then possible to take equation 30, describing the continuous probability density functional in the Fourier space and express its equivalent for a discrete distribution:

$$P(\tilde{f}(\mathbf{k}_1), \tilde{f}(\mathbf{k}_2), \dots) = N \exp \left( -\frac{1}{2} \sum_i \frac{\tilde{f}(\mathbf{k}_i)}{P(\mathbf{k}_i)} \right) = \prod_i C_i \exp \left( -\frac{1}{2} \frac{\tilde{f}(\mathbf{k}_i)}{P(\mathbf{k}_i)} \right). \quad (32)$$

Looking at the discrete distribution in figure 32, it is possible to see that each Fourier mode is in itself a independent normal distribution with  $\mu = 0$  and  $\sigma = \sqrt{P(|\mathbf{k}|)}$ , which means  $C_i = 1/\sqrt{2\pi P(\mathbf{k}_i)}$ . Using this a GRF can be generated by multiplying the Fourier transform of white noise with the square root of the power spectrum [27].

This can be translated into a computer algorithm where we start by generating a white noise realization ( $n_w(\mathbf{q})$ ) in the normal space, consisting of an independent distribution of normal numbers in the lattice we are considering. The Fourier transform of this can be achieve using a FFT algorithm ( $\tilde{n}_w(\mathbf{k}) = FFT(n_w(\mathbf{q}))$ ). To obtain the Fourier modes of the desired GRF, one needs to rescale the modes of the white noise, so they acquire the right standard deviation. This is achieved by multiplying the FFT of the white noise with the square root of the power spectrum ( $\tilde{f}(\mathbf{k}) = \tilde{n}_w(\mathbf{k}) \sqrt{P(\mathbf{k})}$ ). Lastly performing and inverse Fourier transform of the resulting field ( $f(\mathbf{q}) = FFT^{-1}[\tilde{f}(\mathbf{k})]$ ) returns a GRF with the properties desired [27].

Figure 3 shows an example of different Gaussian Random field realizations for different power spectra, this exemplifies how the nature of a GRF can be completely encoded on its power spectrum. The challenge now is to find one that reflects the conditions we want to study.

### 3.1.3 Moments of a Gaussian Random field

The moments of a Gaussian random field ( $E[f(\mathbf{q})]$ ) help describe its statistical properties [29], which will be helpful when studying non-gaussianities. The moments for a general continuous distribution can be described as:

$$E[X^n] = \int X^n f(X) dX . \quad (33)$$

In general, the moments can be obtained from the Moment Generating Function (MGF), such that  $\frac{\partial^n}{\partial t^n} MGF(t)|_{t=0} = E[X^n]$ . For a Gaussian normal distribution, we can define its moment generating function as  $MGF_X(t) = E[e^{tX}]$ . Generalizing these concepts for a Gaussian random field then becomes trivial, instead of considering the normal distribution, consider the probability density functional in a discrete distribution:

$$P(f_1, \dots, f_n) = N \exp \left( -\frac{1}{2} \sum_i \sum_j f_i K_{ij} f_j \right) = N \exp \left( -\frac{1}{2} \mathbf{f}^T K^{-1} \mathbf{f} \right) , \quad (34)$$

where  $K$  is the covariance matrix, corresponding to the two-point correlation function between the two fields and  $\mathbf{f}$  represents the space of all possible Gaussian random fields. Using this form, it is possible to calculate the momentum generating function  $M$ .

$$M(t_1, t_2, \dots, t_n) = E[\exp(\mathbf{t}^T \mathbf{f})] = \exp \left( \frac{1}{2} \sum_i \sum_j t_i K_{ij} t_j \right) . \quad (35)$$

From the equation for  $M$ , it is possible to derive the formula for the moments:

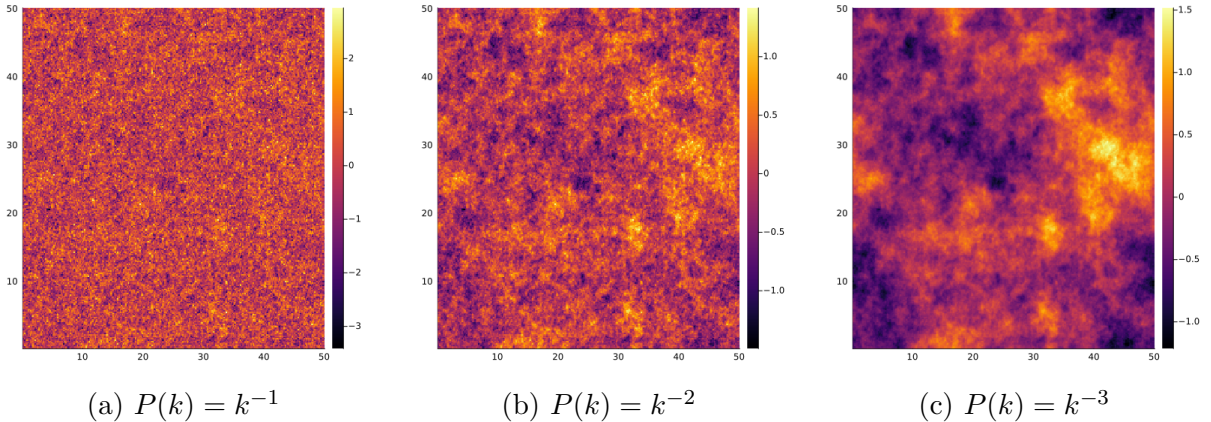


Figure 3: Example of 2D Gaussian Random Fields generated by different power spectra.

$$E[f_i, f_j, \dots, f_n] = \langle f_i, f_j, \dots, f_n \rangle = \frac{\partial^n M}{\partial_i \partial_j \dots \partial_n} \Big|_{t_i, t_j, \dots, t_n=0}. \quad (36)$$

Using this formula for  $E[f_i, f_i] = \langle f_i, f_i \rangle$  we can check if we obtain the covariance matrix as expected earlier:

$$E[f_i, f_j] = \frac{\partial^2}{\partial t_i \partial t_j} \exp\left(\frac{1}{2} \mathbf{t}^T K \mathbf{t}\right) \Big|_{t_i, t_j=0} = K_{ij} = \langle f_i, f_j \rangle, \quad (37)$$

where  $K_{ij} = \varepsilon(\mathbf{f}_1, \mathbf{f}_2)$ , as expected. The results for higher moments of a GRF can be simplified by applying Wick's theorem [30]. This states that every odd correlation function of a Gaussian random field vanishes, while every even correlation function can be described as the sum of all possible two-point correlation function contractions (a more detailed proof of the Wick's theorem for the first moments of a Gaussian random field can be found in Appendix A).

## 3.2 Non-Gaussian Random Fields

Non-Gaussian Random fields can be obtained by the application of non-linear operations in GRFs (for example, eigenvalue fields, are non-Gaussian random fields), in general these can be described as:

$$\Phi = \phi + f_{NL} K[\phi, \phi], \quad (38)$$

where  $\phi$  is a GRF,  $f_{NL}$  parametrizes the amplitudes of the non-gaussianities and  $K[\phi, \phi]$  is an unknown kernel. This report will study Local, Equilateral and Orthogonal non-gaussianities.

### 3.2.1 Local Non-Gaussianities

Local Non-Gaussianities are the simplest form of non-gaussianities and serve as a good example to illustrate different concepts used when dealing with more complex cases. The field representation of local non-gaussianities is given by [31]:

$$\Phi_{Local} = \phi + f_{NL} ([\phi]^2 - \langle \phi^2 \rangle). \quad (39)$$

However, similarly to how the Power Spectrum contains all the information encoded in a Gaussian Random field, Non-Gaussian Random fields can be described in terms of their Bispectrum. The Bispectrum is defined as the fourier transform of the 3-Point Correlation function, such that [32]:

$$\begin{aligned} \langle \tilde{f}(\mathbf{k}_1) \tilde{f}(\mathbf{k}_2) \tilde{f}(\mathbf{k}_3) \rangle &= \int d\mathbf{x} d\mathbf{y} d\mathbf{z} \exp(-i(\mathbf{k}_1 \cdot \mathbf{x} + \mathbf{k}_2 \cdot \mathbf{y} + \mathbf{k}_3 \cdot \mathbf{z})) \langle f(\mathbf{x}) f(\mathbf{y}) f(\mathbf{z}) \rangle \quad (40) \\ &= (2\pi)^3 \delta(\mathbf{k}_1 + \mathbf{k}_2 + \mathbf{k}_3) B(\mathbf{k}_1, \mathbf{k}_2, \mathbf{k}_3), \end{aligned}$$

where  $f$  is just an arbitrary field and  $B(\mathbf{k}_1, \mathbf{k}_2, \mathbf{k}_3)$  is the Bispectrum. It is then possible to construct the Bispectrum for a local non-gaussian field as described in Equation 39.

$$\begin{aligned} \langle \tilde{\Phi}(\mathbf{k}_1) \tilde{\Phi}(\mathbf{k}_2) \tilde{\Phi}(\mathbf{k}_3) \rangle &= \\ &= \langle \phi(\mathbf{k}_1) \phi(\mathbf{k}_2) \phi(\mathbf{k}_3) \rangle \\ &+ f_{NL} \left\langle \left( \phi(\mathbf{k}_1) \phi(\mathbf{k}_3) \left( \int d\mathbf{x} e^{i\mathbf{k}_2 \cdot \mathbf{x}} \phi^2(\mathbf{x}) \right) \right) \right. \\ &\quad \left. + \left( \phi(\mathbf{k}_1) \phi(\mathbf{k}_2) \left( \int d\mathbf{x} e^{i\mathbf{k}_3 \cdot \mathbf{x}} \phi^2(\mathbf{x}) \right) \right) + \left( \phi(\mathbf{k}_2) \phi(\mathbf{k}_3) \left( \int d\mathbf{x} e^{i\mathbf{k}_1 \cdot \mathbf{x}} \phi^2(\mathbf{x}) \right) \right) \right\rangle . \end{aligned} \quad (41)$$

Equation 41 shows the Bispectrum for a Local Non-Gaussian field, where  $\tilde{\phi} = \phi(\mathbf{k})$ , for notation simplicity. Using the Wick's and the convolution theorems it is possible to simplify some of its terms:

$$\langle \phi(\mathbf{k}_1) \phi(\mathbf{k}_2) \phi(\mathbf{k}_3) \rangle = 0 . \quad (42)$$

$$\int d\mathbf{x} e^{i\mathbf{k} \cdot \mathbf{x}} \phi^2(\mathbf{x}) = \text{FT}[\phi^2] = \int \frac{d^3 \mathbf{q}}{(2\pi)^3} \phi(\mathbf{q} - \mathbf{k}) \phi(\mathbf{q}) . \quad (43)$$

Using this results gives then a simplified Bispectrum:

$$\begin{aligned} \langle \tilde{\Phi}(\mathbf{k}_1) \tilde{\Phi}(\mathbf{k}_2) \tilde{\Phi}(\mathbf{k}_3) \rangle &= \\ &= f_{NL} \int \frac{d^3 \mathbf{q}}{(2\pi)^3} (\langle \phi(\mathbf{q}) \phi(\mathbf{q} - \mathbf{k}_1) \phi(\mathbf{k}_2) \phi(\mathbf{k}_3) \rangle + \text{Cycle}) \quad (45) \\ &= 2f_{NL} (\delta(\mathbf{k}_1 + \mathbf{k}_2 + \mathbf{k}_3) P_{\mathbf{k}_1} P_{\mathbf{k}_2} + \text{Cycle}) . \quad (46) \end{aligned}$$

Equation 46 shows how the Bispectrum can be described in terms of the cycle permutations of the power spectrum, "Cycle" in this equation refers to the cyclic permutations of  $\mathbf{k}_i$  that were omitted in order to simplify the expression. From this equality, it is possible to conclude that the Bispectrum for local non-Gaussianities is given by [31]:

$$B_{\Phi}^{local} = 2f_{NL} P_1 P_2 + \text{Cycle} , \quad (47)$$

where  $P_{\mathbf{k}_i} = P_i$

### 3.2.2 Field Reconstruction

While the operation to calculate a Bispectrum from a parent field seems straightforward, the opposite is not true. Deducing a field from a Bispectrum is complicated since the kernel represents the relationship between two modes of the same field, while the Bispectrum represents the sum of the averages between the cyclic permutations of the Power Spectrum [31]. Consequently most of the literature available deals directly with the Bispectrum by employing methods like Fisher Matrices Algorithms to study it [33–35]. However, this is not an option for this project since our application depends directly

on our capacity to generate an initial non-gaussian field to simulate the primordial density field. Here we will explain how non-gaussianities can be derived using the inversion method proposed by Scoccimarro et all [31] to find a way to reproduce the kernel for each type of non-Gaussianity.

Firstly, it is necessary to find a generic form for the kernel in Fourier space, this can be inferred from equation 38 [31]:

$$\tilde{\Phi}(\mathbf{k}) = \tilde{\phi}(\mathbf{k}) + f_{NL} \text{FT}[K[\phi, \phi]]. \quad (48)$$

The kernel is considered to be quadratic and non-local, such that its Fourier transform can be given by [13]:

$$\tilde{\Phi}(\mathbf{k}) = \tilde{\phi}(\mathbf{k}) + f_{NL} \iint d\mathbf{k}_1^3 d\mathbf{k}_2^3 \delta(\mathbf{k} - (\mathbf{k}_1 + \mathbf{k}_2)) \tilde{K}[\mathbf{k}_1, \mathbf{k}_2, \mathbf{k}] \phi(\mathbf{k}_1) \phi(\mathbf{k}_2), \quad (49)$$

where  $\tilde{K}[\mathbf{k}_1, \mathbf{k}_2, \mathbf{k}]$  is the Fourier Transform of the Kernel. Following the process described in section 3.2.1, the following formula for the generic Bispectrum can be found:

$$B_{\Phi}^{Gen} = 2f_{NL} \tilde{K}_{12} P_1 P_2 + \text{Cycle}, \quad (50)$$

with  $\tilde{K}_{12} = \tilde{K}[\mathbf{k}_1, \mathbf{k}_2, \mathbf{k}]$  and  $P_i = P(\mathbf{k}_i)$

Looking at the general form of the Bispectrum, it is easy to see that the main property to be conserved across different kernels is its  $\mathbf{k}_1 \leftrightarrow \mathbf{k}_2$  symmetry.

$$\frac{1}{6f_{NL}} B_{\Phi}^{Eq} = -(P_1 P_2 + \text{Cycle}) - 2(P_1 P_2 P_3)^{\frac{2}{3}} + (P_1^{\frac{1}{3}} P_2^{\frac{2}{3}} P_3 + \text{Cycle}). \quad (51)$$

$$\frac{1}{6f_{NL}} B_{\Phi}^{Ort} = -3(P_1 P_2 + \text{Cycle}) - 8(P_1 P_2 P_3)^{\frac{2}{3}} + 3(P_1^{\frac{1}{3}} P_2^{\frac{2}{3}} P_3 + \text{Cycle}). \quad (52)$$

Equations 51 and 52 present the Bispectrum for Equilateral and Orthogonal Non-Gaussian fields [1]. Looking at the different types of Bispectra, it is possible to identify 3 different types of subterms we need to solve: a local type subterm,  $(P_1 P_2 + \text{Cycle})$ ; a  $6(P_1 P_2 P_3)^{\frac{2}{3}}$  subterm which will be called term A; and a  $(P_1^{\frac{1}{3}} P_2^{\frac{2}{3}} P_3 + \text{Cycle})$  subterm, term B. Solving each term individually will provide the tools to find the forms for the types of non-gaussianities being studied.

Before inverting the Bispectra, there is one more approximation to consider. The Power Spectrum used must be scale invariant and described as  $P(\mathbf{k}) \propto k^{-n}$ , where n can be any natural number and  $k = |\mathbf{k}|$ . We will consider the case for  $n = 3$  since this will be greatly simplify the proofs being done, however this method can be generalized for any natural n [31].

### Local Term:

For the Local term we consider the following equality:

$$2f_{NL} \tilde{K}_{12} P_1 P_2 + \text{Cycle} = 2f_{NL} P_1 P_2 + \text{Cycle}. \quad (53)$$

In general a kernel can have the form:

$$(P_1^{-\alpha} P_2^{-\beta} + P_2^{-\alpha} P_1^{-\beta}) P_3^{-(2-\alpha-\beta)}, \quad (54)$$

where  $\alpha$  and  $\beta$  are arbitrary constants that can be tuned to fit the equality 53. There are two solutions for the form in Equation 54 that could satisfy this equality, one where  $\alpha = \beta = 1$ , meaning  $\tilde{K} = 1$  and a case where  $\alpha = 1$  and  $\beta = 0$ , returning a kernel:

$$\tilde{K}_{12} = \frac{P_3}{2} \left( \frac{1}{P_1} + \frac{1}{P_2} \right), \quad (55)$$

since this will generate the same final Bispectrum:

$$2f_{NL}\tilde{K}_{12}P_1P_2 + Cycle = 2f_{NL}\frac{P_3}{2} \left( \frac{1}{P_1} + \frac{1}{P_2} \right) P_1P_2 + Cycle = 2f_{NL}P_1P_2 + Cycle. \quad (56)$$

Combining the two possible solutions, we get the final kernel [31]:

$$\tilde{K}_{12}^{Local} = (1-u) + u \frac{P_3}{2} \left( \frac{1}{P_1} + \frac{1}{P_2} \right), \quad (57)$$

where  $u$  is an arbitrary that weights the different contributions to the kernel. For  $u = 0$ , we can see how the Kernel will generate the Bispectrum for the Local Non-Gaussianities discussed earlier, so  $u$  can be interpreted as a measure of the locality. The final field is given by taking the inverse Fourier transform of the Fourier Space Kernel:

$$K[\phi, \phi] = FT^{-1} \left[ \iint d\mathbf{k}_1^3 d\mathbf{k}_2^3 \delta(\mathbf{k} - (\mathbf{k}_1 + \mathbf{k}_2)) \tilde{K}[\mathbf{k}_1, \mathbf{k}_2] \phi(\mathbf{k}_1) \phi(\mathbf{k}_2) \right]. \quad (58)$$

Knowing that  $P(\mathbf{k}) \propto k^{-3}$ , it is possible to infer several relations between the Fourier Space expressions and what they mean in real space, namely that every factor of  $k$  can be translated into a differential operator:

$$\begin{aligned} \partial\phi(\mathbf{x}) &= \int e^{-i\mathbf{k.x}} k \phi(\mathbf{k}) d^3k, & \nabla^{-2}\phi &= - \int e^{-i\mathbf{k.x}} k^{-2} \phi(\mathbf{k}) d^3k, \\ \partial^{-1}\phi(\mathbf{x}) &= \int e^{-i\mathbf{k.x}} k^{-1} \phi(\mathbf{k}) d^3k. \end{aligned} \quad (59)$$

Using this properties, it is possible to obtain the real space field expression for this term [31]:

$$\Phi^{Local} = \phi + f_{NL} [(1-u)\phi^2 + u\nabla^{-2}\partial^{-1}(\phi\nabla^2\partial\phi)]. \quad (60)$$

## Term A

For term A, the following equality can be considered:

$$2f_{NL}\tilde{K}_{12}P_1P_2 + Cycle = 6(P_1P_2P_3)^{\frac{2}{3}}. \quad (61)$$

There is only one possible solution in this case,  $\alpha = \beta = \frac{2}{3}$ , which generates a kernel:

$$\tilde{K}_{12}^A = \frac{P_3^{2/3}}{(P_1 P_2)^{1/3}}. \quad (62)$$

such that :

$$2f_{NL}\tilde{K}_{12}P_1P_2 + Cycle = 2f_{NL}\frac{P_3^{2/3}}{(P_1 P_2)^{1/3}} = 2f_{NL} \cdot 3(P_1 P_2 P_3)^{\frac{2}{3}}. \quad (63)$$

Using the same inversion method as before, the following final field can be found [31]:

$$\Phi^A = \phi - f_{NL}\nabla^{-2}(\partial\phi)^2. \quad (64)$$

## Term B

Lastly, for term B, the following equality must be obeyed:

$$2f_{NL}\tilde{K}_{12}P_1P_2 + Cycle = 2f_{NL}(P_1^{\frac{1}{3}}P_2^{\frac{2}{3}}P_3 + Cycle), \quad (65)$$

using the  $\mathbf{k}_1 \leftrightarrow \mathbf{k}_2$  symmetry, there are 3 possible solutions for term 54 :  $\alpha = \frac{2}{3}$ ,  $\beta = 1$ ;  $\alpha = \frac{1}{3}$ ,  $\beta = 1$  and  $\alpha = \frac{1}{3}$ ,  $\beta = \frac{2}{3}$ . This will generate 3 different possible kernels [31]:

$$\tilde{K}_{12}^1 = P_3^{1/3}(P_1^{-1/3} + P_2^{-1/3}). \quad (66)$$

$$\tilde{K}_{12}^2 = P_3(P_1^{-2/3}P_2^{-1/3} + P_2^{-2/3}P_1^{-1/3}). \quad (67)$$

$$\tilde{K}_{12}^3 = P_3^{1/3}(P_1^{-1/3} + P_2^{-1/3}). \quad (68)$$

summing the 3 different contributions gives the overall kernel [31]:

$$\tilde{K}_{12}^B = (1 - s - t)\tilde{K}_{12}^1 + s\tilde{K}_{12}^2 + t\tilde{K}_{12}^3, \quad (69)$$

where s and t are constants to give relative weights to each kernel. The total kernel can now be inverted to find the final field [31]:

$$\Phi^B = \phi + f_{NL}[(1 - s - t)\partial^{-1}(\phi\partial\phi) + t\nabla^{-2}(\phi\nabla^2\phi) + s(\nabla^{-2}\partial^{-1}(\nabla^2\phi\partial\phi))]. \quad (70)$$

### 3.2.3 Equilateral and Orthogonal Non-Gaussianities

The Kernel corresponding to each type of non-gaussianity can be written as a combination of the 3 terms described previously [31]:

$$\tilde{K}_{12}^{Eq} = -3\tilde{K}_{12}^{Local} - 2\tilde{K}_{12}^A + 3\tilde{K}_{12}^B. \quad (71)$$

$$\tilde{K}_{12}^{Ort} = -9\tilde{K}_{12}^{Local} - 8\tilde{K}_{12}^A + 9\tilde{K}_{12}^B. \quad (72)$$

However there is still one aspect that needs to be solved, the parameters  $u, s$  and  $t$  that deal with the different Kernel component weights. The choice of this variables involves considering the changes in the Power Spectrum caused by the non-gaussianities and try to correct for them in a way that the low  $k$  the behavior of the power spectrum remains  $P_\Phi(\mathbf{k}) \propto k^{-3}$  (meaning that for large distances the Power Spectrum is still gaussian). However these corrections are beyond the scope of this project and as such we will just refer to the results from [31]. To ensure that at low  $k$ , a factor of  $k^{-3}$  dominates, we must define  $u = s = 0$  for both non-gaussianities and  $t = \frac{1}{3}$  for equilateral fields and  $t = \frac{4}{9}$  for equilateral fields. This originates the following field templates [31]:

$$\Phi_{Eq} = \phi + f_{NL} [-3\phi^2 + 4\partial^{-1}(\phi\partial\phi) + 2\nabla^{-2}(\phi\nabla^2\phi) + 2\nabla^{-2}(\partial\phi)^2] . \quad (73)$$

$$\Phi_{Ort} = \phi + f_{NL} [-9\phi^2 + 10\partial^{-1}(\phi\partial\phi) + 8\nabla^{-2}(\phi\nabla^2\phi) + 8\nabla^{-2}(\partial\phi)^2] . \quad (74)$$

These non-gaussianities can then be generated through computational methods by using Fast Fourier Transforms to generate the Fourier transform of  $\phi$  and performing the differential operations in Fourier space (as described in equation 59).

## 4 Caustic Theory

As discussed in section 2, the cosmic web can be separated into different multi-stream regions, separated by caustics, regions of infinite density. Having understood how to generate non-gaussian random fields, it is now important to understand how to map and identify the different types of caustics. This can be done best by employing the density field generated by the Zel'dovich approximation:

$$\rho(\mathbf{q}, t) = \frac{\bar{\rho}(t)}{|(1 + D_+(t)\alpha(\mathbf{q}))(1 + D_+(t)\beta(\mathbf{q}))|} , \quad (20)$$

where  $\alpha$  and  $\beta$  are the eigenvalues of the deformation tensor. Having looked at this from the perspective of the density field, it is also important to consider how caustics are seen in position space :

$$\mathbf{x}(\mathbf{q}, D_+(t)) = \mathbf{q} + D_+(t)\mathbf{s}(\mathbf{q}) . \quad (14)$$

Figure 4 shows the evolution through time of a dark matter sheet under the effect of gravity (obeying equation 14), showing how the Lagrangian (initial coordinates) space will project into the Eulerian (final coordinates) space. This exemplifies how the boundaries between multi-stream regions will correspond to singularities in the density field as well as introducing how momentary singularities are formed as the sheet folds to create a multistream region.

To understand how caustics are formed, one must remember that we treat dark as a fluid. The regions of infinite density exist because when a mass element of the fluid moves between different stream regions, it will go through an infinitely small boundary, while having a non-zero mass, causing the local density to spike to infinity. This change between different stream regions is called shell crossing. To identify the different types of caustics formed, it is then necessary to understand what conditions must a given element

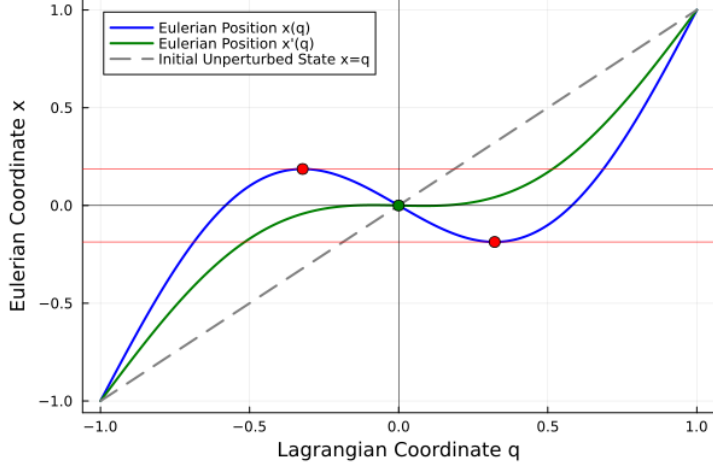


Figure 4: 1D representation of a Dark Matter sheet (line in 1D) undergoing evolution under the Zel'dovich approximation. The blue line represents sheet with a 1-stream and a 3-stream region, with the red lines representing the boundaries of the 3-stream region in Eulerian space. The red dots represent the boundary of this region in the dark matter sheet and will correspond to points of infinite density. The green line corresponds to the moment right before a 3-stream region is formed, where the green dot represents the inflection point where several points in the Eulerian space  $q$  correspond to the same final coordinate  $x'(q)$ , this will also correspond to a point of infinite density.

of the fluid fulfill to undergo shell crossing at a given point in time, the shell crossing conditions.

## 4.1 Shell Crossing Conditions

Considering a 2D dark matter sheet, shell crossing will happen when two mass elements in Lagrangian space correspond to the same point in Eulerian space [16]:

$$\frac{\Delta \mathbf{x}}{|\Delta \mathbf{q}|} = \frac{|\mathbf{x}_t(\mathbf{q}') - \mathbf{x}_t(\mathbf{q}'')|}{|\mathbf{q}' - \mathbf{q}''|} \rightarrow 0 \quad \text{as } \mathbf{q}', \mathbf{q}'' \rightarrow \mathbf{q}_s. \quad (75)$$

where  $\mathbf{q}_s$  is the critical point, the point where a singularity will occur in the density field. This can be interpreted as having a curve in Lagrangian space that gets deformed until the points in both side of  $\mathbf{q}_s$  in Eulerian space start coinciding, like shown in figure 5. This means that the point  $\mathbf{x}_t(\mathbf{q}_s)$  will be discontinuous, meaning that during shell crossing the the partial derivative of  $\mathbf{x}_t$ , will vanish along the tangential direction to the shell crossing curve ,  $\mathbf{T}$ .

$$\left| \frac{\partial \mathbf{x}_t}{\partial \mathbf{q}} \cdot \mathbf{T} \right| = 0 \Leftrightarrow \left| \mathbf{T} + \frac{\partial \mathbf{s}_t}{\partial \mathbf{q}} \cdot \mathbf{T} \right| = 0, \quad (76)$$

where  $\frac{\partial \mathbf{s}_t}{\partial \mathbf{q}}$  is the time-dependent deformation tensor  $M$  with  $\mathbf{s}_t(\mathbf{q}) = -D_+(t)\nabla_{\mathbf{q}}\Psi(\mathbf{q})$ . This is the same as demanding [16]:

$$\mathbf{T} + M \cdot \mathbf{T} = 0. \quad (77)$$

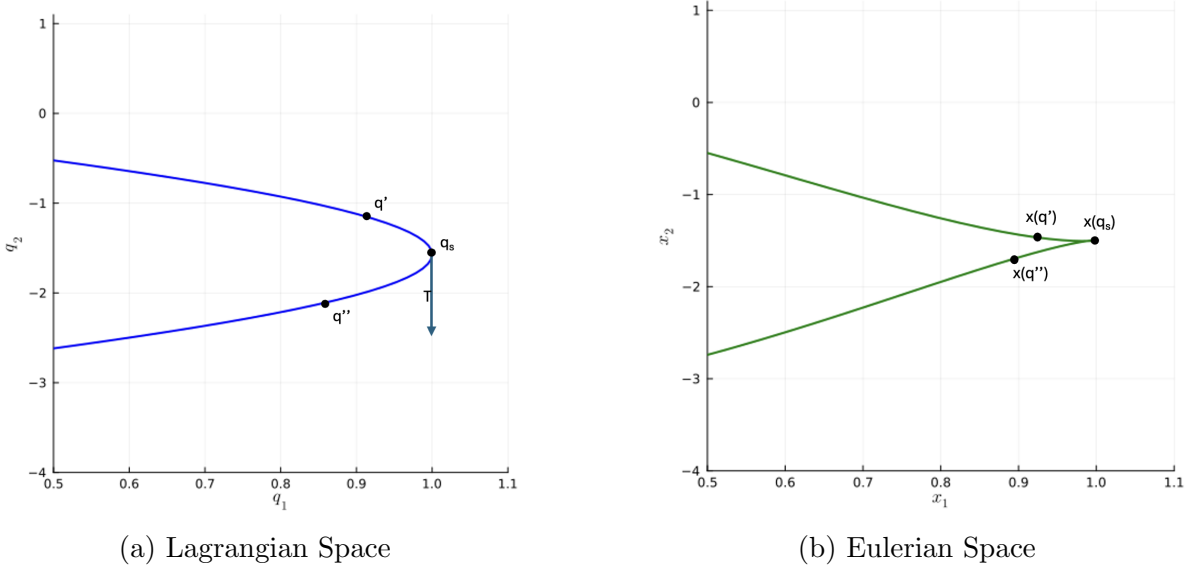


Figure 5: Example of a shell crossing in 2D

Diagonalizing  $M$ , will help further simplify this equation, defining:

$$M_d = \begin{pmatrix} \mu_{1,t} & 0 \\ 0 & \mu_{2,t} \end{pmatrix}, \quad V = \begin{pmatrix} v_{11} & v_{21} \\ v_{12} & v_{22} \end{pmatrix}, \quad (78)$$

where  $M_d$  is the diagonal deformation tensor,  $\mu_{it} = D_+(t)\mu_i$  are the time-dependent eigenvalues and  $V$  is the eigenvector matrix  $V = (\mathbf{v}_1, \mathbf{v}_2)$ , where  $\mathbf{v}_1, \mathbf{v}_2$  are the eigenvectors, allowing to rewrite the condition in Equation 76 as:

$$\mathbf{T} + M \cdot \mathbf{T} = V(T + M \cdot \mathbf{T})V^{-1} = V(I + M_d)V^{-1} \cdot \mathbf{T} = (I + M)V^{-1} \cdot \mathbf{T} = 0, \quad (79)$$

where  $V^{-1} = \begin{pmatrix} \mathbf{v}_1^* \\ \mathbf{v}_2^* \end{pmatrix}$  and  $MV = M_dV$ . Similarly  $\mathbf{T}$  can be defined as  $\mathbf{T} = \nabla\mu_{it}(\mathbf{q}_s)$ , since the gradient always points towards the direction of steepest increase, which will necessarily be tangential to the curve along which shell crossing is occurring. Finally, it is possible to get the following shell-crossing conditions [16]:

$$\begin{pmatrix} (1 + \mu_{1,t})\mathbf{v}_{1t}^* \cdot \nabla\mu_{it}(\mathbf{q}_s) \\ (1 + \mu_{2,t})\mathbf{v}_{2t}^* \cdot \nabla\mu_{it}(\mathbf{q}_s) \end{pmatrix} = 0. \quad (80)$$

From this, we can conclude that a point  $\mathbf{q}_s$  will undergo shell crossing if there exists at least one eigenvalue ( $\mu_{it}$ ) or eigenvector ( $\mathbf{v}_{it}$ ) that obeys the following conditions:

$$1 + \mu_{it}(\mathbf{q}_s) = 0 \quad OR \quad \mathbf{v}_{it}(\mathbf{q}_s)^* \cdot \nabla\mu_{it}(\mathbf{q}_s) = 0 \quad (81)$$

## 4.2 Caustic Conditions

Caustic families are defined by the number of shell crossing conditions they obey. The A caustic family represents the caustics that only involve one of the eigenvalues or eigen-

vectors, while the D family caustics represents the family whose conditions involve both eigenvalues or eigenvectors [16]. The caustic families work in an hierachic manner, where the next caustic of a family must obey all the conditions imposed on the caustics before them and new one. In a 2D space there are 4 possible different types of caustics  $A_2$ ,  $A_3$ ,  $A_4$  and  $D_4$ . To implement the caustic skeleton method we now need to establish the relation between these caustics and the cosmic web.

The  $A_2$  caustic, also called the fold caustic is the simplest that can be formed, in 2D this represents a closed line that encompasses a multi-stream region, these represent the lines along which shell crossing is occurring, indicating collapsed regions of space [17]. These caustics are represented by the red dots in figure 4, and the blue lines in figure 6. The  $A_2$  lines, that indicate the fold caustics occurring, must obey the following condition:

$$A_2^i(t) = \{\mathbf{q} \in L : 1 + \mu_{it}(\mathbf{q}) = 0\} \quad (82)$$

for  $i = 1, 2$  corresponding to the number of spacial dimensions and  $L$  indicating the Lagrangian space.

The  $A_3$  cusp caustics obey the same condition as the  $A_2$  but have one extra restriction: they only occur when the isocontour defined by the  $A_2$  line is perpendicular to the eigenvector. This returns the following condition:

$$A_3^i(t) = \{q \in L : 1 + \mu_{it}(\mathbf{q}) = 0 \wedge \mathbf{v}_{it}(\mathbf{q}) \cdot \nabla \mu_{it}(\mathbf{q}) = 0\} \quad (83)$$

The  $A_3$  caustics (in 2D) mark a kink in the boundary between two different multi-stream regions, this can be seen at the interception between the  $A_3$  and  $A_2$  lines. The  $A_3$  lines indicate the points that have formed cusps until that point in time, and will correspond to a filament of the cosmic web [17]. In 1D these correspond to the momentarily formed caustic marked by the green point in figure 4 while in 2D cusps can be seen at the interceptions of the red ( $A_3$ ) and blue ( $A_2$ ) lines in figure 6.

The higher order  $A_4$  swallowtail caustic occurs at the points where the  $A_3$  lines are perpendicular to the eigenvector field, obeying a further restriction given by:

$$\begin{aligned} A_4^i(t) = \{\mathbf{q} \in L : & 1 + \mu_{it}(\mathbf{q}) = 0 \wedge \mathbf{v}_{it}(\mathbf{q}) \cdot \nabla \mu_{it}(\mathbf{q}) = 0 \\ & \wedge \mathbf{v}_{it}(\mathbf{q}) \cdot \nabla(\mathbf{v}_{it}(\mathbf{q}) \cdot \nabla \mu_{it}(\mathbf{q})) = 0\} \end{aligned} \quad (84)$$

Lastly, the  $D_4$  caustics are defined by the points where the eigenvalue fields coincide:

$$D_4(t) = \{q \in L : 1 + \mu_{1t}(\mathbf{q}) = 0 \wedge 1 + \mu_{2t}(\mathbf{q}) = 0\} \quad (85)$$

Both the  $A_4$  and  $D_4$  correspond to extra spikes in the density field, indicating clusters or knots in the cosmic web [17], however, the goal of this project is to provide a first look at the effects of non-gaussianites on structure formation and not an in-depth look at it, as such the analysis performed will focus only on  $A_2$  and  $A_3$  structures since these are more indicative of the general topology of the field. This mainly empirical derivation of caustic conditions reflects a deeper connection with Catastrophe theory, presented in Appendix B to provide more information about the nature of caustics.

### 4.3 Computing Caustics

The Caustic Skeleton method consists on the implementation of the caustics conditions to study structure formation in the cosmic web. The code used to find the caustics in an initial density field can be found in Appendix C, however, we will provide a brief overview of the methods and parameters used. Firstly, the power spectrum of the field used to generate the initial density perturbations is given by [17]:

$$P(k) = N k^{n-4} e^{-R_s^2 k^2} \quad (86)$$

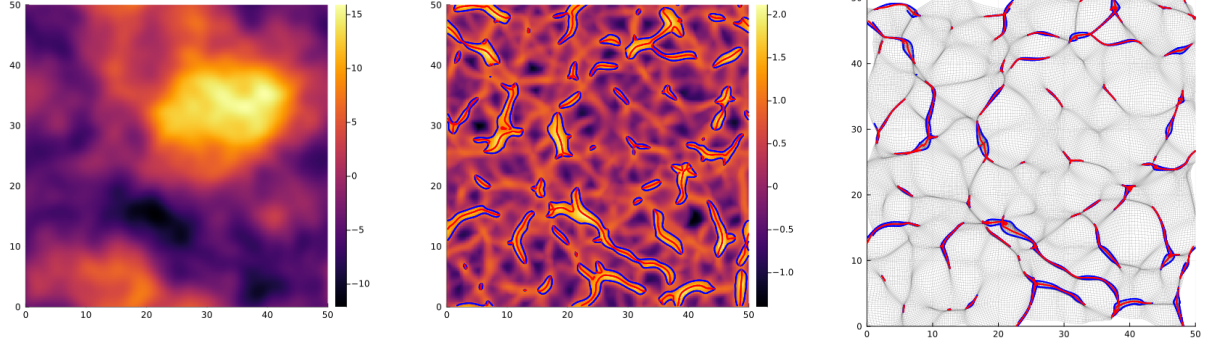
where  $R_s$  is the cut-off length that helps smoothing off the field and  $N$  is a normalization constant, helping to set the amplitude of the field fluctuations ( $\delta$ ) to  $\langle \delta^2 \rangle = \alpha^2$  and can be given by:

$$N = \frac{\alpha^2 4\pi R_s^{n-2}}{\Gamma(1 + \frac{n}{2})} \quad (87)$$

where  $\Gamma$  is the gamma function. In our simulations we used  $n = 1$ , in order to keep the validity of the derivations in section 3.2.2,  $\alpha = 1$  and  $R_s = 1$ . Considering we are performing 2D simulations, these were kept unitless considering they don't have any physical significance regardless.

To identify the different caustics, one starts by generating the eigenvalue and eigenvector fields. To identify the  $A_2$  lines, the eigenvalue field is put through the caustic condition described in Equation 82, separating the results from this in a grid, it is possible to identify adjacent points with a sign change and use it to extrapolate the zero crossing points where the caustics will occur. A similar method is employed when calculating the  $A_3$  caustics, but considering the scalar product between the eigenvector field and the gradient of the eigenvalue field (obeying the conditions in Equation 83). However, one extra precaution must be taken when generating the tangential vector, calculating the gradient of the eigenvalue field will generate vectors in both the positive and negative tangential direction, making it difficult to identify the zero crossing points, since our method is sensitive to sign changes. To solve this the tangential vectors need to be locally aligned for every region of the grid being studied.

Figure 6 presents the results from this method, where from the initial density field (Figure 6(a)), it is possible to use the eigenvalue field to identify the underlying caustic skeleton (Figure 6(b)) and find how this caustics behave in Eulerian space (Figure 6(c)).

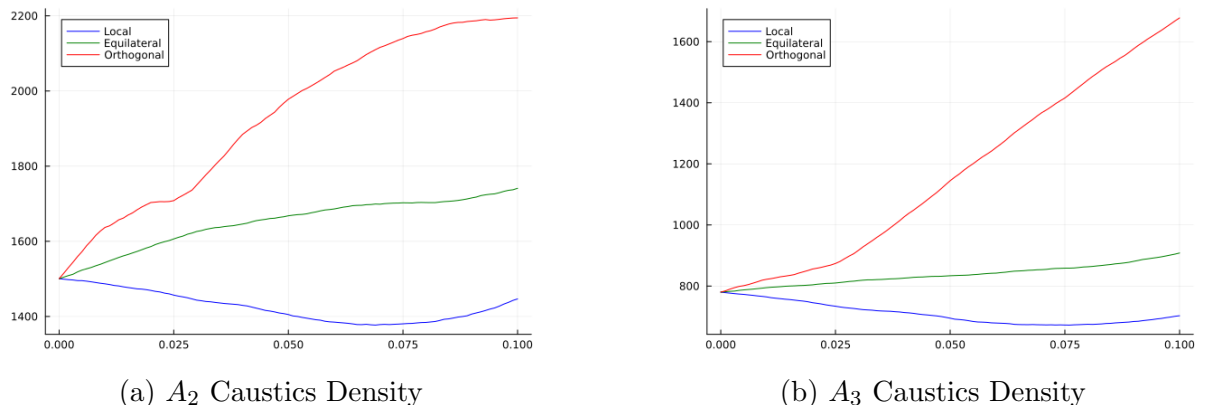


(a) Primordial Density Field      (b) First Eigenvalue Field      (c) Eulerian Space Caustics

Figure 6: Simulation of the Caustic Skeleton based on a Gaussian Random field. The blue lines show the  $A_2$  caustics generated by the first eigenvalue field, bounding the different mass elements that when through shell crossing. The cusp caustics can be seen at the interceptions between the  $A_2$  lines and while the red lines indicating the  $A_3$  lines, these will correspond to filaments.

## 5 Caustics and non-Gaussianities

Using the forms derived in Section 3.2 it is possible to study the impact of different non-gaussianites for different values of  $f_{NL}$ . Figure 7 shows an analysis into how the caustics number density (number of points corresponding to an  $A_2$  or  $A_3$  caustic in a 256 by 256 field) changes for different types of non-gaussianities and values of  $f_{NL}$ . Since this is a mathematical study that deals in unitless quantities, the range of  $f_{NL}$  used doesn't correspond to the values usually encountered in the literature [1]. From this analysis, it is possible to conclude that different types of non-gaussianities produce different density profiles from  $f_{NL} \approx 0.001$ , meaning it is possible to use the caustic number density to distinguish between different types of non-gaussianities. This is a crude approach that doesn't tell much about the changes in the geometry of the cosmic web, as such, it is also relevant to study how specific field implementations react.



(a)  $A_2$  Caustics Density

(b)  $A_3$  Caustics Density

Figure 7: Average Caustics Number Density for Non-Gaussian fields generated from 100 different realizations of a Gaussian Random field of length 10.

Figures 8, 9 and 10 show the caustics in both the eigenvalue field and Eulerian space for Local, Equilateral and Orthogonal non-gaussian fields, all based on the same starting gaussian field of  $L = 10$ . The caustics given by the first eigenvalue field are represented by the blue ( $A_2$ ) and red ( $A_3$ ) lines. The ranges of  $f_{NL}$  vary slightly between each type in order to illustrate the similarities and differences between the field's dependence on  $f_{NL}$ . Comparing the results between different non-gaussianities, there are some aspects of notice, first, they all produce small but visible changes from  $f_{NL} \approx 0.001$ , although these are not visible in the resolution of the figures presented here. Furthermore all different non-gaussianities produce visibility different results from each other. Secondly, it is possible to see that different non-gaussianities scale differently with  $f_{NL}$ , namely Orthogonal non-gaussianities produce much more noticeable distortions for smaller values of  $f_{NL}$  when compared to the fields produced by the other non-gaussianities at the same values. All these conclusions are in agreement to what can be observed in the caustics density graphs. Appendix D presents the Eulerian field evolution for a field with  $L=50$ , further corroborating our findings.

Overall the most interesting results are for low values of  $f_{NL}$ , since since we expect the initial density field to be very close to gaussianity thus, it is these small, but noticeable changes that must be studied.

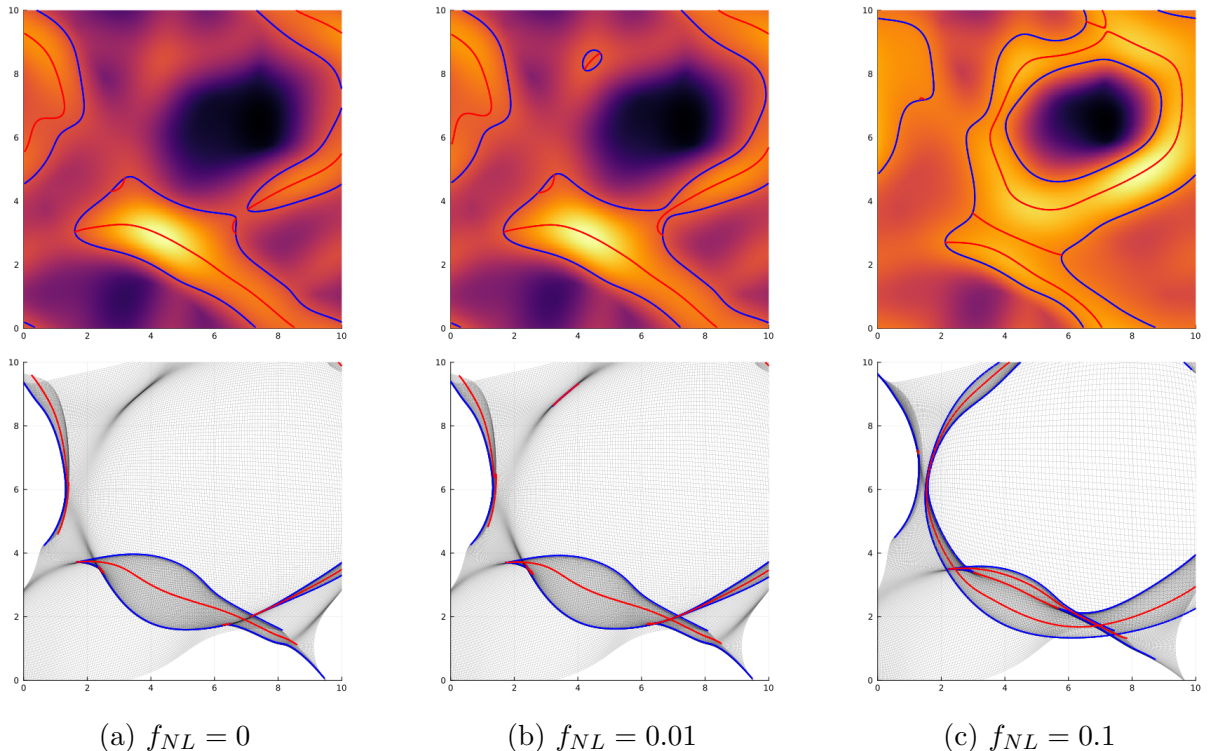


Figure 8: Local Non-gaussianities for a field of lenght 10, in both the first eigenvalue field (1<sup>st</sup> row) and Eulerian Space (2<sup>nd</sup> row) for different values of  $f_{NL}$

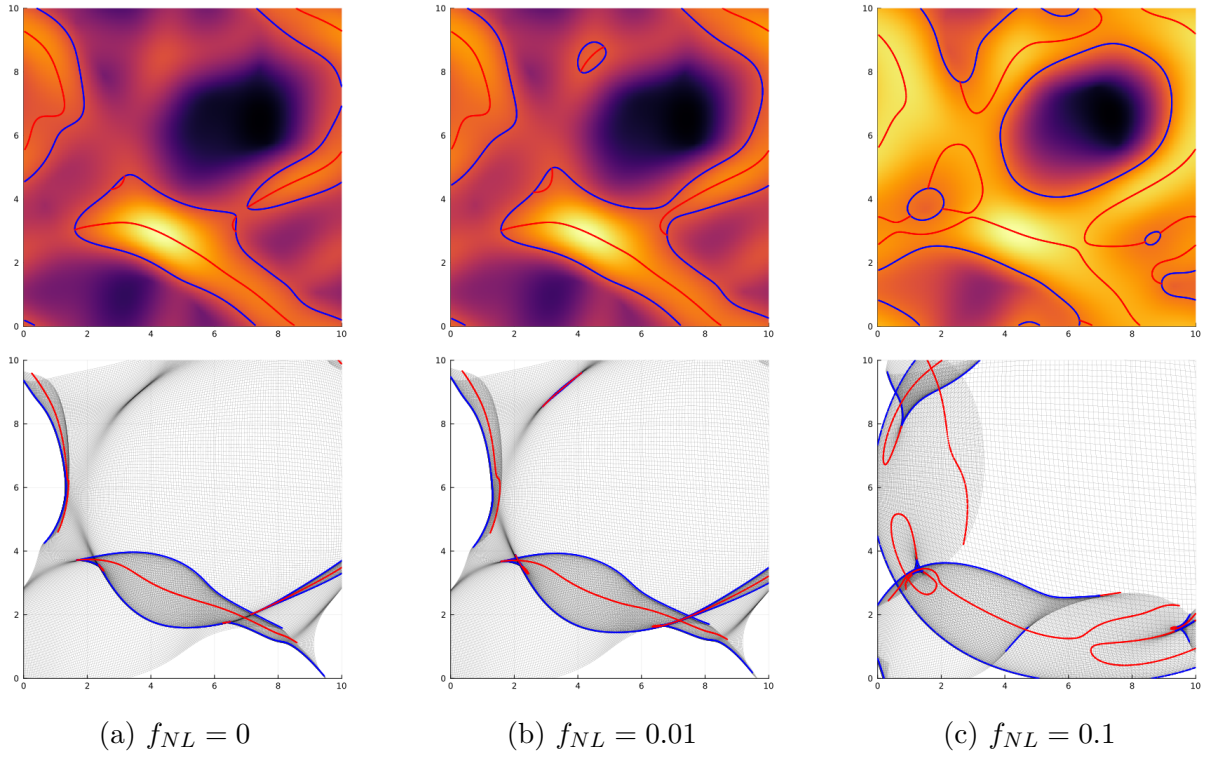


Figure 9: Equilateral Non-gaussianities for a field of lenght 10, in both the first eigenvalue field (1<sup>st</sup> row) and Eulerian Space (2<sup>nd</sup> row) for different values of  $f_{NL}$

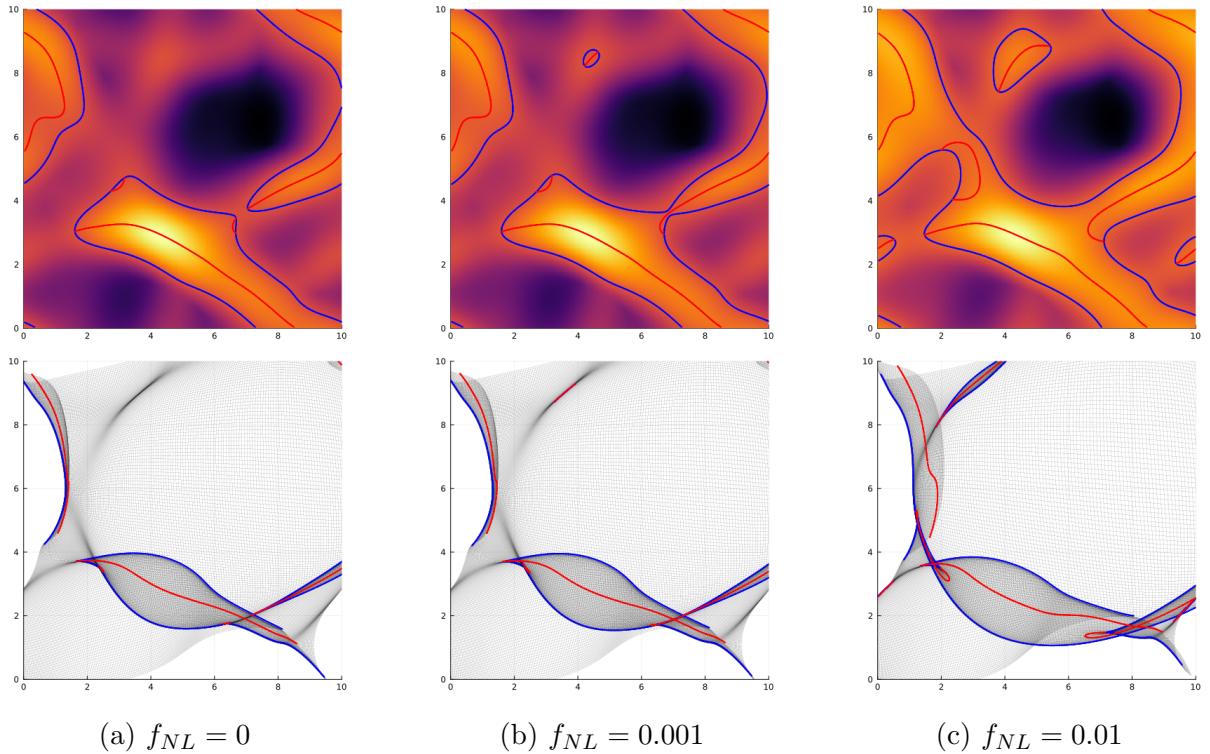


Figure 10: Orthogonal Non-gaussianities for a field of lenght 10, in both the first eigenvalue field (1<sup>st</sup> row) and Eulerian Space (2<sup>nd</sup> row) for different values of  $f_{NL}$

## 6 Discussion & Conclusion

This project has successfully implemented a method to study non-gaussianities in the cosmic web using the Caustic Skeleton method. Using the inversion procedure proposed by Scocciamaro et all [31], it is possible to generate realizations of non-gaussian primordial density fields. By applying the Zel'dovich approximation, the geometry of the cosmic web can be studied through the caustics formed at the boundaries of different multi-stream regions. Although neither of these methods is new, this was the first time they were combined into a mathematical study of the properties of the caustics formed by Local, Orthogonal and Equilateral non-gaussian fields. This allows us to conclude that the Caustic Skeleton method can be used to successfully identify the different types of non-gaussianities, since these produce both different caustic densities across different field realizations and visibly different structures when studying a specific field, even for a small value of  $f_{NL}$ .

Future developments should focus on the strengths which employing the study of caustics presents. The main advantage of using the Caustic Skeleton method is that by allowing the construction our own field realizations, it is possible to use constraint gaussian fields to generate specific structures and thus study them in more detail [17, 27]. Applying these to see how specific structures of the cosmic web, like filaments, react under different non-gaussian primordial fields would help increase our understanding of structure formation. Similarly, a future study must provide a more in depth analysis into how the caustics density changes with non-gaussianites, going beyond the point density method used in this project. An approach to study the caustics density would be to implement a method based on the Kac-Rice formula ([36, 37]), that allows for the calculation of the number of times a gaussian field crosses a given threshold or point, and apply it in the context of the cosmic web and for non-gaussian fields. Lastly, future developments in this method must also focus on bringing this analysis beyond a purely mathematical study and into a physical simulation of the 3D cosmic web, finding ways this process can be integrated with experimental observables like measures of the CMB Bispectrum [38].

In conclusion this project has shown that the Caustic Skeleton is a promising new method to study primordial non-gaussianities. This can be expanded through several avenues and hopefully reveal a new way to learn more about early universe physics.

## References

1. Pettinari, G. W. *The Intrinsic Bispectrum of the Cosmic Microwave Background* ISBN: 978-3-319-21881-6 978-3-319-21882-3. <https://link.springer.com/10.1007/978-3-319-21882-3> (2025) (Springer International Publishing, Cham, 2016).
2. Rotti, A., Ravenni, A. & Chluba, J. Non-Gaussianity constraints with anisotropic distortion measurements from *Planck*. *Monthly Notices of the Royal Astronomical Society* **515**, 5847–5868. ISSN: 0035-8711, 1365-2966. <https://academic.oup.com/mnras/article/515/4/5847/6651389> (2025) (Aug. 19, 2022).
3. information@eso.org. *The Cosmic Web (Artist's Impression)* [www.esahubble.org](http://www.esahubble.org). <https://www.esahubble.org/images/heic2003b/> (2025).

4. *Planck CMB* [https://www.esa.int/ESA\\_Multimedia/Images/2013/03/Planck\\_CMB](https://www.esa.int/ESA_Multimedia/Images/2013/03/Planck_CMB) (2025).
5. Komatsu, E. *et al.* *Non-Gaussianity as a Probe of the Physics of the Primordial Universe and the Astrophysics of the Low Redshift Universe* Apr. 19, 2009. arXiv: 0902.4759[astro-ph]. <http://arxiv.org/abs/0902.4759> (2025).
6. Desjacques, V. & Seljak, U. Primordial Non-Gaussianity in the Large-Scale Structure of the Universe. *Advances in Astronomy* **2010** (ed Huterer, D.) 908640. ISSN: 1687-7969, 1687-7977. <https://onlinelibrary.wiley.com/doi/10.1155/2010/908640> (2025) (Jan. 2010).
7. Komatsu, E. & Spergel, D. N. *The cosmic microwave background bispectrum as a test of the physics of inflation and probe of the astrophysics of the low-redshift universe* in *The Ninth Marcel Grossmann Meeting* (Dec. 2002), 2009–2010. arXiv: astro-ph/0012197. <http://arxiv.org/abs/astro-ph/0012197> (2025).
8. Bernui, A. & Rebouças, M. J. Non-Gaussianity in the foreground-reduced CMB maps. *Physical Review D* **81**, 063533. ISSN: 1550-7998, 1550-2368. <https://link.aps.org/doi/10.1103/PhysRevD.81.063533> (2025) (Mar. 30, 2010).
9. Bernui, A. & Rebouças, M. J. Mapping possible non-Gaussianity in the *Planck* maps. *Astronomy & Astrophysics* **573**, A114. ISSN: 0004-6361, 1432-0746. <http://www.aanda.org/10.1051/0004-6361/201424654> (2025) (Jan. 2015).
10. Hernández-Aguayo, C. *et al.* The MillenniumTNG Project: High-precision predictions for matter clustering and halo statistics. *Monthly Notices of the Royal Astronomical Society* **524**, 2556–2578. ISSN: 0035-8711, 1365-2966. arXiv: 2210.10059[astro-ph]. <http://arxiv.org/abs/2210.10059> (2025) (July 12, 2023).
11. Gabrielpillai, A. *et al.* Galaxy formation in the Santa Cruz semi-analytic model compared with IllustrisTNG – I. Galaxy scaling relations, dispersions, and residuals at  $z = 0$ . *Monthly Notices of the Royal Astronomical Society* **517**, 6091–6111. ISSN: 0035-8711, 1365-2966. <https://academic.oup.com/mnras/article/517/4/6091/6674219> (2025) (Nov. 12, 2022).
12. Villaescusa-Navarro, F. *et al.* The Quijote simulations. *The Astrophysical Journal Supplement Series* **250**, 2. ISSN: 0067-0049, 1538-4365. arXiv: 1909.05273[astro-ph]. <http://arxiv.org/abs/1909.05273> (2025) (Sept. 1, 2020).
13. Coulton, W. R. *et al.* Quijote-PNG: Simulations of primordial non-Gaussianity and the information content of the matter field power spectrum and bispectrum. *The Astrophysical Journal* **943**, 64. ISSN: 0004-637X, 1538-4357. arXiv: 2206.01619[astro-ph]. <http://arxiv.org/abs/2206.01619> (2025) (Jan. 1, 2023).
14. Gutiérrez Adame, A. *et al.* PNG-UNITsims: Halo clustering response to primordial non-Gaussianities as a function of mass. *Astronomy & Astrophysics* **689**, A69. ISSN: 0004-6361, 1432-0746. [https://www.aanda.org/10.1051/0004-6361/202349037](http://www.aanda.org/10.1051/0004-6361/202349037) (2025) (Sept. 2024).
15. Baldi, M. *et al.* Cosmological simulations of scale-dependent primordial non-Gaussianity. *Journal of Cosmology and Astroparticle Physics* **2024**, 053. ISSN: 1475-7516. [http://iopscience.iop.org/article/10.1088/1475-7516/2024/11/053](https://iopscience.iop.org/article/10.1088/1475-7516/2024/11/053) (2025) (Nov. 1, 2024).

16. Feldbrugge, J., van de Weygaert, R., Hidding, J. & Feldbrugge, J. Caustic Skeleton & Cosmic Web. *Journal of Cosmology and Astroparticle Physics* **2018**, 027–027. ISSN: 1475-7516. arXiv: 1703.09598 [astro-ph, physics:physics]. <http://arxiv.org/abs/1703.09598> (2024) (May 8, 2018).
17. Feldbrugge, J. L. & Weygaert, R. *What makes a cosmic filament? The dynamical origin and identity of filaments I. fundamentals in 2D* in (May 30, 2024). <https://www.semanticscholar.org/paper/What-makes-a-cosmic-filament-The-dynamical-origin-Feldbrugge-Weygaert/6250c7575e541da2f1b26587479ecd581a1d8365> (2025).
18. Dodelson, S. *Modern cosmology* Nachdr. 440 pp. ISBN: 978-0-12-219141-1 (Academic Press, Amsterdam).
19. Arbey, A. & Mahmoudi, F. Dark matter and the early Universe: A review. *Progress in Particle and Nuclear Physics* **119**, 103865. ISSN: 01466410. <https://linkinghub.elsevier.com/retrieve/pii/S0146641021000193> (2025) (July 2021).
20. Ryden, B. *Introduction to Cosmology* 2nd ed. ISBN: 978-1-316-65108-7 (Cambridge University Press, 2016).
21. David Weinberg. *A8873 Cosmology Course Notes : VIII. Linear Fluctuations* 2024. <https://www.astronomy.ohio-state.edu/weinberg.21/A8873/a8873.html>.
22. Klypin, A. & Holtzman, J. Particle mesh code for cosmological simulations. *arXiv: Astrophysics*. <https://www.semanticscholar.org/paper/b2615c9536774ce85b1873c99e7c222b595e11d0> (2025) (Dec. 17, 1997).
23. Hidding, J. *jhidding/nbody2d: 2d PM n-body code* version v0.1.0. Oct. 30, 2020. <https://zenodo.org/records/4158731> (2025).
24. Arnold, V. I., Shandarin, S. F. & Zeldovich, Y. B. The large scale structure of the universe I. General properties. One-and two-dimensional models. *Geophysical & Astrophysical Fluid Dynamics* **20**, 111–130. ISSN: 0309-1929, 1029-0419. <http://www.tandfonline.com/doi/abs/10.1080/03091928208209001> (2024) (Apr. 1982).
25. Hidding, J., Shandarin, S. F. & van de Weygaert, R. The Zeldovich approximation: key to understanding Cosmic Web complexity. *Monthly Notices of the Royal Astronomical Society* **437**, 3442–3472. ISSN: 0035-8711, 1365-2966. arXiv: 1311.7134 [astro-ph]. <http://arxiv.org/abs/1311.7134> (2024) (Feb. 1, 2014).
26. Hamilton, A. J. S. Formulae for growth factors in expanding universes containing matter and a cosmological constant. *Monthly Notices of the Royal Astronomical Society* **322**, 419–425. ISSN: 0035-8711, 1365-2966. <https://academic.oup.com/mnras/article/322/2/419/963632> (2025) (Apr. 1, 2001).
27. Feldbrugge, J. & Weygaert, R. v. d. Cosmic Web & Caustic Skeleton: non-linear Constrained Realizations – 2D case studies. *Journal of Cosmology and Astroparticle Physics* **2023**, 058. ISSN: 1475-7516. arXiv: 2212.07840 [astro-ph]. <http://arxiv.org/abs/2212.07840> (2025) (Feb. 1, 2023).
28. Feldbrugge, J. L. *Statistics of Caustics in Large-Scale Structure Formation* PhD thesis (June 2014). [https://jfeldbrugge.github.io/Job\\_Feldbrugge\\_files/Literature/masterthesis.pdf](https://jfeldbrugge.github.io/Job_Feldbrugge_files/Literature/masterthesis.pdf) (2025).

29. Riley, K. F., Bence, S. J. & Hobson, M. P. *Mathematical Methods for Physics and Engineering: A Comprehensive Guide* 3rd ed. DOI: <https://doi.org/10.1017/{CBO}9780511810763>. 1359 pp. ISBN: 978-0-521-67971-8. <https://doi.org/10.1017/CBO9780511810763> (Cambridge University Press, Cambridge, 2006).
30. Wick, G. C. The Evaluation of the Collision Matrix. *Physical Review* **80**, 268–272. ISSN: 0031-899X. <https://link.aps.org/doi/10.1103/PhysRev.80.268> (2025) (Oct. 15, 1950).
31. Scoccimarro, R., Hui, L., Manera, M. & Chan, K. C. Large-scale Bias and Efficient Generation of Initial Conditions for Non-Local Primordial Non-Gaussianity. *Physical Review D* **85**, 083002. ISSN: 1550-7998, 1550-2368. arXiv: 1108.5512[astro-ph]. <http://arxiv.org/abs/1108.5512> (2025) (Apr. 4, 2012).
32. Ivanov, M. M. *et al.* Cosmology with the Galaxy Bispectrum Multipoles: Optimal Estimation and Application to BOSS Data. *Physical Review D* **107**, 083515. ISSN: 2470-0010, 2470-0029. arXiv: 2302.04414[astro-ph]. <http://arxiv.org/abs/2302.04414> (2025) (Apr. 17, 2023).
33. Smith, K. M. & Zaldarriaga, M. Algorithms for bispectra: forecasting, optimal analysis, and simulation. *Monthly Notices of the Royal Astronomical Society* **417**, 2–19. ISSN: 00358711. arXiv: astro-ph/0612571. <http://arxiv.org/abs/astro-ph/0612571> (2025) (Oct. 11, 2011).
34. Smith, K. M., Senatore, L. & Zaldarriaga, M. *Optimal analysis of the CMB trispectrum* Feb. 2, 2015. arXiv: 1502.00635[astro-ph]. <http://arxiv.org/abs/1502.00635> (2025).
35. Lewis, A. *The real shape of non-Gaussianities* Mar. 14, 2012. arXiv: 1107.5431[astro-ph]. <http://arxiv.org/abs/1107.5431> (2025).
36. Feliu, E. & Sadeghimanesh, A. Kac-Rice formulas and the number of solutions of parametrized systems of polynomial equations. *Mathematics of Computation*. ISSN: 0025-5718, 1088-6842. <https://www.ams.org/mcom/0000-000-00/S0025-5718-2022-03760-1/> (2025) (Aug. 11, 2022).
37. Stecconi, M. Kac-Rice formula for transverse intersections. *Analysis and Mathematical Physics* **12**, 44. ISSN: 1664-2368, 1664-235X. <https://link.springer.com/10.1007/s13324-022-00654-0> (2025) (Apr. 2022).
38. Hill, J. C. Foreground biases on primordial non-Gaussianity measurements from the CMB temperature bispectrum: Implications for *Planck* and beyond. *Physical Review D* **98**, 083542. ISSN: 2470-0010, 2470-0029. <https://link.aps.org/doi/10.1103/PhysRevD.98.083542> (2025) (Oct. 31, 2018).
39. Saunders, P. T. *An Introduction to Catastrophe Theory* ISBN: 978-0-521-23042-1. <https://www.cambridge.org/core/books/an-introduction-to-catastrophe-theory/D5ECA839997CD9C2A247C413E69CD2B8> (2025) (Cambridge University Press, Cambridge, 1980).
40. Gupta, M. K., Bansal, K. & Singh, A. K. Mass and Length Dependent Chaotic Behavior of a Double Pendulum. *IFAC Proceedings Volumes* **47**, 297–301. ISSN: 14746670. <https://linkinghub.elsevier.com/retrieve/pii/S1474667016326714> (2025) (2014).

## A Wick's Theorem

Section 3.1.3 presented Wick's theorem and how for a Gaussian random field odd correlation functions vanish while even correlation functions can be described as the sum of all possible two-point correlation functions contractions. Here we prove this for the third and fourth momentum of a Gaussian Random field so the generalisation of this concept becomes more obvious.

The three-point correlation function is given by:

$$\begin{aligned} E[f_i, f_j, f_k] &= \frac{\partial}{\partial t_k} \left( K_{ij} + \left( \sum_m t_m K_{im} \right) \left( \sum_m t_m K_{jm} \right) \right) M \Big|_{t_i, t_j, t_k=0} \\ &= \left[ 0 + K_{ik} \left( \sum_m t_m K_{jm} \right) + K_{jk} \left( \sum_m t_m K_{im} \right) \right] M \Big|_{t_i, t_j, t_k=0} \\ &+ \left[ \left( K_{ij} + \left( \sum_m t_m K_{im} \right) \left( \sum_m t_m K_{jm} \right) \right) \left( \sum_m t_m K_{km} \right) \right] M \Big|_{t_i, t_j, t_k=0} = 0 \end{aligned} \quad (88)$$

Similarly the 4-point correlation function can be calculated as well:

$$\begin{aligned} E[f_i, f_j, f_k, f_l] &\quad (89) \\ &= \frac{\partial}{\partial t_l} \left\{ \left[ K_{ik} \left( \sum_m t_m K_{jm} \right) + K_{jk} \left( \sum_m t_m K_{im} \right) \right] M \right\} \Big|_{t_i, t_j, t_k, t_l=0} \\ &+ \frac{\partial}{\partial t_l} \left\{ \left[ \left( K_{ij} + \left( \sum_m t_m K_{im} \right) \left( \sum_m t_m K_{jm} \right) \right) \left( \sum_m t_m K_{km} \right) \right] M \right\} \Big|_{t_i, t_j, t_k, t_l=0} \\ &= [K_{ik} K_{jl} + K_{jk} K_{il}] M \Big|_{t_i, t_j, t_k, t_l=0} \quad (91) \\ &\quad \left[ K_{ik} \left( \sum_m t_m K_{jm} \right) + K_{jk} \left( \sum_m t_m K_{im} \right) \right] \left( \sum_m t_m K_{lm} \right) M \Big|_{t_i, t_j, t_k, t_l=0} \\ &+ \left[ \left( K_{ij} + \left( \sum_m t_m K_{im} \right) \left( \sum_m t_m K_{jm} \right) \right) \left( \sum_m t_m K_{km} \right) \right] \left( \sum_m t_m K_{lm} \right) M \Big|_{t_i, t_j, t_k, t_l=0} \\ &\quad + \left[ \left( K_{ij} + \left( \sum_m t_m K_{im} \right) \left( \sum_m t_m K_{jm} \right) \right) K_{kl} \right] M \Big|_{t_i, t_j, t_k, t_l=0} \\ &+ \left[ \left( K_{il} \left( \sum_m t_m K_{jm} \right) + \left( \sum_m t_m K_{im} \right) K_{jl} \right) \left( \sum_m t_m K_{km} \right) \right] M \Big|_{t_i, t_j, t_k, t_l=0} \\ &= K_{ik} K_{jl} + K_{jk} K_{il} + K_{ij} K_{kl} \quad (92) \end{aligned}$$

It is then clear how these results can be extended to infinity to proof the wick's theorem.

## B Catastrophe Theory

Catastrophe theory focuses on the study and classification of critical points [39]. A critical point of a function  $f(\mathbf{x})$  can be defined as the points where:

$$\nabla f(\mathbf{x})|_{x_0} = 0. \quad (93)$$

Similarly to what is done for a single variable function, the nature of a singularity can be classified depending on the nature of its second derivative. Generalizing this for higher dimensions, the nature of the critical point is defined by its Hessian ( $H_{ij}(f(\mathbf{x})) = \partial_i \partial_j f(\mathbf{x})$ ). A point is said to be **degenerate** if the  $\det(H(f(\mathbf{x}))) = 0$ , however a vanishing determinant doesn't imply a vanishing second derivative for all the variables of  $f(\mathbf{x})$ .

To classify a degenerate critical point, one only needs to consider its essential variables, those for which the second derivative is always zero independently of their coordinate frame (as stated by the splitting theorem). These correspond to the zero eigenvalues of the Hessian, being that the number of essential variables is called the co-rank of the singularity.

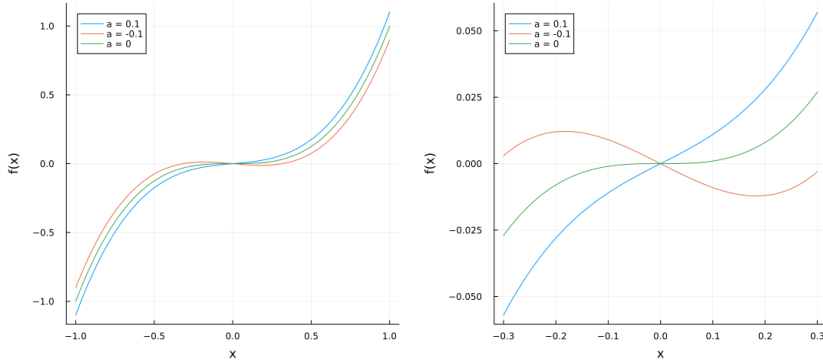


Figure 11: Example of Structurally Unstable function,  $f(x) = x^3 - ax$ , the factor  $ax$  unfolds the degenerate critical point at the origin into two non-degenerate critical points.

To understand the importance of studying the behavior of critical points, one must first understand the concept of **structural stability** [39]. This concept can be better illustrated with an example from science, when performing a scientific experiment, we expect most systems to return approximately the same result if they are under approximately the same initial conditions (a small, almost infinitesimal change in initial conditions like temperature, pressure, location will produce an equally small change in the final results), these systems are then structurally stable. However this is not the case for all systems, chaotic systems are defined as systems highly sensible to changes in initial conditions. The double pendulum is one of the most famous examples of such cases, where a small change in its initial release position generates a completely different trajectory [40]. These systems are thus not structurally stable. Structural stability can then be defined as the ability of a system to keep its nature under a small perturbation.

The same concept can be applied to a mathematical context. In this case, we consider a function, for example, a polynomial  $x^n$ , if adding any term of the form  $ax^m$ , for any small  $a$  and natural  $m$ , doesn't change the nature of the function near its critical point

then the function is structurally stable. Structural stability can then be extended to a family of functions, using as an example the case described in Figure 11,  $f(x) = x^3$  is not structurally stable since the addition of the term  $ax$  changes its character, however, the family of functions  $f_a(x) = x^3 - ax$  defined by the parameter  $a$ , is structurally stable since the addition of any  $bx^m$  won't change its behavior near the critical point.

A degenerate critical point is by nature unstable, this can be seen as a point that has several different coincidental critical points that need to be separated, this can be done by adding some small perturbations that displace some of the critical points away from the origin, this process is called unfolding [39]. A good example to explain this is  $x^4$ , adding an extra  $ax^2$  term will generate a family of functions with a maximum at the origin and minima at  $x = \sqrt{-a/2}$ , for  $a < 0$ , however, this family will still be unstable since the addition of a small term  $bx$  can still alter the function type. The new function  $F_{a,b} = x^4 + ax^2 + bx$ , is stable since the addition of any other  $x^m$  term will not change its behaviour near the origin.

Structurally stable foldings are called versals, while a versal folding with the minimum number of parameters for it to be stable is called universal, **the universal unfolding of a singularity is unique** [39]. The minimum number of parameters for a universal unfolding is given by the number of the first non-vanishing derivatives after the second one. A critical point with an n-parameters universal unfolding is said to be an n-fold degenerate critical point. The number of parameters of the universal unfolding is also called the **codimension** of a singularity.

Although this method has been only established for polynomials, this is not problematic, since it focuses on studying only a critical point of a function, meaning that as long as the function being studied is smooth, it can be Taylor expanded around that point, thus making this method widely applicable. Although the example used to illustrate the concepts was done in one dimension, this can be generalized to an N-dimension space [39].

## B.1 The Elementary Catastrophes in 2D

The elemental catastrophes correspond to the all the unique unfoldings that can exist for all the possible singularities in a given space. As established before, a universal unfolding is unique and all functions can be reduced to a Taylor expansion around the singular point. In 2D, we are restricted to unfoldings of codimension 3, and at most 2 essential variables in each unfolding. This means that there can only exist 5 unique singularities and thus 5 unique unfoldings.

$$x^3, x^4, x^5; x^3 - xy^2, x^3 + y^3 \quad (94)$$

Equation 94 shows the list of unique singularities in the 2D space, the first caustic study is the  $A_2$  fold caustic,  $x^3$ . The universal unfolding is given by  $f_{A_2}(x) = x^3 + ax$ , to find the allowed parameter space for  $a$  is given by the values of  $a$  for which the first derivative vanishes and that satisfy  $\det[H(f_{A_2}(x))] = 0$ , generating a system of equation that returns the  $a = 0$ . In this case, the  $A_2$  catastrophe corresponds only to a point in parameter space.

Similarly, for the next singularity, the  $A_3$  Cusp Catastrophe,  $x^4$ , the unfolding is straightforward,  $f_{A_4}(x) = x^4 + ax^2 + bx$ , similarly the parameter space will be given by

the equation  $8a^3 + 37v^2$ . The same approach can be taken to find the other catastrophes parameter space, however, these won't be relevant for this project, and as such these are omitted. Table 1 shows the Elementary catastrophes and their respective unfoldings for completeness.

Class	Name	Singularity	Universal Unfolding
$A_2$	Fold	$x^3$	$x^3 + ax$
$A_3$	Cusp	$x^4$	$x^4 + ax^2 + bx$
$A_4$	Swallowtail	$x^5$	$x^5 + ax^3 + bx^2 + cx$
$D_4^-$	Elliptic Umbilic	$x^3 - xy^2$	$x^3 - xy^2 + a(x^2 + y^2) + bx + cy$
$D_4^+$	Hyperbolic Umbilic	$x^3 + y^3$	$x^3 + y^3 + axy + bx + cy$

Table 1: Elementary Catastrophes in a 2D space

## B.2 Catastrophe theory in the Cosmic Web

Having explained how we can study a critical point, and the different types of catastrophes, it is now necessary to understand the physicality of the methods used, mainly what do essential variables and parameters mean in the context of the Zel'dovich approximation. The Zel'dovich approximation studies the evolution of mass points from Lagrangian to Eulerian space, this leads us to conclude that its essential variables will be its Lagrangian space coordinates, while its parameters must be the Eulerian space coordinates [25]. This means that for 2D simulations like the ones used for this project, we are limited to a 3-parameter space ( $x_1$ ,  $x_2$  and  $t$ , since the final Eulerian space depends on both the spatial coordinates and the time at which it is observed). Similarly the caustics we observe in our universe correspond to the parameter space coordinates that allow for the unfolding of a critical point and the shapes we observe are caused by the restrictions imposed on the parameters by the unfolding.

To give a better intuition about how the caustics arrive as degenerate critical points of the cosmic web, we consider the displacement potential origination of the Zel'dovich approximation,  $\mathbf{x}(q) = \nabla F$ , such that:

$$F(\mathbf{q}) = \frac{(\mathbf{q} - \mathbf{x})^2}{2} + \Psi(\mathbf{q}), \quad (95)$$

where  $\Psi = D_+(t) \frac{2}{3\Omega_0 H_0^2} \phi_0(\mathbf{q})$ . It is possible to conclude that both the red and green points in Figure 4 are degenerate critical points of  $F(\mathbf{q})$ , obeying the following equations:

$$\frac{\partial F}{\partial \mathbf{q}_i} = 0 \Leftrightarrow \mathbf{x}(\mathbf{q}) = \mathbf{q} + \nabla \Psi \quad (96)$$

$$\left| \frac{\partial F}{\partial \mathbf{q}_i \partial \mathbf{q}_j} \right| = 0 \Leftrightarrow |I + M| = (1 + u_{1t})(1 + u_{2t}) = 0 \quad (97)$$

where  $M$  is the time-dependent deformation tensor, with eigenvalues  $u_{it}$ . Equation 96 recovers the Zel'dovich approximation we have been applying and Equation 97, returns the conditions for singularities in the density field. The duality between the different catastrophes and the different caustics here studied becomes now clear.

## C Project Code

Here we leave snippets of the Julia code used to generate the simulations used in this project. This was based on the initial inputs provided by Job Feldbrudge.

```
1 using FFTW, Plots, Revise, ProgressMeter, Random,
  SpecialFunctions, Distributions, Interpolations, StaticArrays
  , LinearAlgebra, Measures, Base.Threads, DelimitedFiles
```

Listing 1: Packages Used

```
1 struct GRF
2   L::AbstractFloat
3   Ni::Int
4   kx::Matrix{AbstractFloat}
5   ky::Matrix{AbstractFloat}
6   seed::Int
7   Pk::Matrix{AbstractFloat}
8 end
9
10 function GRF_Init(Ni, L, ns, Rs, alpha, seed)
11   #Range in frequency space
12   kRange(n, L) = fftfreq(n) * n * 2. * pi / L
13   kx = repeat(kRange(Ni, L), 1, Ni)
14   ky = kx'
15   Pk = P.(sqrt.(kx.^2 + ky.^2), ns, Rs, alpha)
16   Pk[1, 1] = 0.
17   return GRF(L, Ni, kx, ky, seed, Pk)
18 end
19
20 #Power spectrum
21 function P(k, ns, Rs, alpha)
22   return alpha^2 * 4. * pi * Rs^(2. + ns) / gamma(1. + ns / 2.)
23   * k^(ns - 4.) * exp(-Rs^2 * k^2)
24 end
25 function GRF_Gen(cgrf::GRF)
26   Random.seed!(cgrf.seed)
27   return real(ifft(sqrt.(cgrf.Pk) .* fft(randn(cgrf.Ni, cgrf.Ni
28   )))) * cgrf.Ni^(2/2) / cgrf.L^(2/2)
```

Listing 2: Gaussian random field generating code

```
1 struct gridcell
2   p::Array
3   eigen_1::Array
4   inner::Array
5   ID::Array
6
7   function gridcell(i, j, eig1, eig1_grad, v1, Range)
```

```

8     points = [
9         Range[i]      Range[j]
10        Range[i + 1] Range[j]
11        Range[i]      Range[j + 1]
12        Range[i + 1] Range[j + 1]]
13
14     eigen_1 = extractCube([i, j], eig1)
15
16     inner = [directional_derivative_1(eig1_grad, v1, i + di,
17                                     j + dj, i, j) for di in 0:1, dj in 0:1][:]
18
19     return new(points, eigen_1, inner, [i, j])
20 end
21
22 #calculate the eigenvalue and eigenvector fields
23 function eigenFields123(hess)
24     Ni = size(hess, 1)
25     eig1 = zeros(Ni, Ni)
26     eig2 = zeros(Ni, Ni)
27     vec1 = zeros(Ni, Ni, 2)
28     vec2 = zeros(Ni, Ni, 2)
29
30     for i in 1:Ni, j in 1:Ni
31         eig = eigen123(hess[i,j,:])
32         eig1[i, j] = eig[1]
33         eig2[i, j] = eig[2]
34         vec1[i, j, :] = eig[3]
35         vec2[i, j, :] = eig[4]
36     end
37     return (eig1, eig2, vec1, vec2)
38 end
39
40 mutable struct CausticSkeleton
41     A2::Vector{Matrix{Float64}}
42     A3::Vector{Matrix{Float64}}
43     function CausticSkeleton()
44         return new(
45             Vector{Matrix{Float64}}(undef, 0),
46             Vector{Matrix{Float64}}(undef, 0))
47     end
48 end
49
50 function extractCube(ID, data)
51     i, j = ID[1], ID[2]
52     return data[i:i+1, j:j+1][:]
53 end
54
55 #Compute the caustics

```

```

56 function Caustics!(hess, iso, cgrf::GRF)
57     skeleton = CausticSkeleton()
58     (eig1, eig2, vec1, vec2) = eigenFields123(hess)
59
60     Ni = cgrf.Ni
61     L = cgrf.L
62     Range = range(0. , L, Ni + 1)[2:end]
63     eig1_grad = grad(eig1, cgrf)
64
65
66     @showprogress for i in 1:Ni-1, j in 1:Ni-1
67         g = gridcell(i, j,eig1, eig1_grad, v1, Range)
68         if any(g.eigen_1 .> iso )
69             PolygoniseA2!(g, skeleton, iso)
70             PolygoniseA!(g, skeleton, iso, eig1_grad, v1)
71         end
72     end
73     return skeleton
74 end
75
76 function PolygoniseA2!(g::gridcell, skeleton::CausticSkeleton,
77     iso)
78     PolygoniseA2!(g, skeleton, iso, [1, 2, 3])
79     PolygoniseA2!(g, skeleton, iso, [1, 3, 4])
80 end
81 #Generate the A2 caustics
82 function PolygoniseA2!(g::gridcell, skeleton::CausticSkeleton,
83     iso, v)
84     triindex = 0
85     if g.eigen_1[v[1]] < iso triindex |= 1 end
86     if g.eigen_1[v[2]] < iso triindex |= 2 end
87     if g.eigen_1[v[3]] < iso triindex |= 4 end
88
89     if triindex == 1 || triindex == 6
90         push!(skeleton.A2, hcat(
91             VertexInterp(iso, g.p[v[1],:], g.p[v[3],:], g.eigen_1
92                 [v[1]], g.eigen_1[v[3]]),
93             VertexInterp(iso, g.p[v[1],:], g.p[v[2],:], g.eigen_1
94                 [v[1]], g.eigen_1[v[2]]))')
95     elseif triindex == 2 || triindex == 5
96         push!(skeleton.A2, hcat(
97             VertexInterp(iso, g.p[v[2],:], g.p[v[1],:], g.eigen_1
98                 [v[2]], g.eigen_1[v[1]]),
99             VertexInterp(iso, g.p[v[2],:], g.p[v[3],:], g.eigen_1
100                [v[2]], g.eigen_1[v[3]]))')
101     elseif triindex == 3 || triindex == 4
102         push!(skeleton.A2, hcat(
103             VertexInterp(iso, g.p[v[1],:], g.p[v[3],:], g.eigen_1
104                 [v[3]], g.eigen_1[v[1]]),
105             VertexInterp(iso, g.p[v[1],:], g.p[v[2],:], g.eigen_1
106                 [v[1]], g.eigen_1[v[2]]))')
107     end
108 end

```

```

99      [v[1]], g.eigen_1[v[3]]),
100     VertexInterp(iso, g.p[v[2],:], g.p[v[3],:], g.eigen_1
101       [v[2]], g.eigen_1[v[3]]))')
102   end
103 end
104 #A3 Caustics
105 function PolygoniseA!(g::gridcell, skeleton::CausticSkeleton, iso
106   , eig1_grad, v1)
107   PolygoniseA!(g, skeleton, iso, [1, 2, 3], eig1_grad, v1)
108   PolygoniseA!(g, skeleton, iso, [1, 3, 4], eig1_grad, v1)
109 end
110 #A3 Caustics
111 function PolygoniseA!(g::gridcell, skeleton::CausticSkeleton, iso
112   , v, eig1_grad, v1)
113   delta = g.p[2,1] - g.p[1,1]
114
115   triindex = 0
116   if g.inner[v[1]] < 0 triindex |= 1 end
117   if g.inner[v[2]] < 0 triindex |= 2 end
118   if g.inner[v[3]] < 0 triindex |= 4 end
119
120   function pushA3(v1, w1, v2, w2)
121     p1 = VertexInterp(0, g.p[v1,:], g.p[w1,:], g.inner[v1], g
122       .inner[w1])
123     p2 = VertexInterp(0, g.p[v2,:], g.p[w2,:], g.inner[v2], g
124       .inner[w2])
125
126     eigen1 = interpolation_cubic(p1, g.eigen_1, delta, g)
127     eigen2 = interpolation_cubic(p2, g.eigen_1, delta, g)
128
129     triindex = 0
130     if eigen1 > iso triindex |= 1 end
131     if eigen2 > iso triindex |= 2 end
132
133     # Screen over lines
134     if triindex == 1
135       pp2 = VertexInterp(iso, p1, p2, eigen1, eigen2)
136       push!(skeleton.A3, hcat(p1, pp2)')
137     elseif triindex == 2
138       pp1 = VertexInterp(iso, p1, p2, eigen1, eigen2)
139       push!(skeleton.A3, hcat(pp1, p2)')
140
141   end

```

```

142     end
143
144     # Screen over triangles
145     if      triindex == 1 || triindex == 6
146         pushA3(v[1], v[3], v[1], v[2])
147     elseif triindex == 2 || triindex == 5
148         pushA3(v[2], v[1], v[2], v[3])
149     elseif triindex == 3 || triindex == 4
150         pushA3(v[1], v[3], v[2], v[3])
151     end
152 end

```

Listing 3: Caustic Finding Code

```

1 #Zel'dovich for positions
2 function Zel'dovich(f, Dp, GRF::GRF, qRange)
3     q_x = qRange
4     q_y = q_x'
5     (s_x, s_y) = (convolve(GRF.kx * im, f),
6                      convolve(GRF.ky * im, f))
7     return stack((q_x .+ Dp .* s_x, q_y .+ Dp .* s_y))
8 end
9
10 # Caustics In Eulerian Space
11 function Eulerian1(simplices, s, cgrf::GRF, Dp )
12     qRange(n, L) = range(0., L, n + 1)[2:end]
13     Range = qRange(cgrf.Ni, cgrf.L)
14     s1_itp = Interpolations.scale(interpolate(s[:, :, 1], BSpline(
15         Linear(Periodic()))), Range, Range)
16     s2_itp = Interpolations.scale(interpolate(s[:, :, 2], BSpline(
17         Linear(Periodic()))), Range, Range)
18     return [EulerianA(sim, s1_itp, s2_itp, Dp) for sim in
19             simplices]
20 end
21
22 function EulerianA(M::Matrix, s1_itp, s2_itp, Dp = 1)
23     return stack([Eulerian2(q, s1_itp, s2_itp, Dp) for q in
24                 eachrow(M)])
25 end
26
27 Eulerian2(q, s1_itp, s2_itp, Dp = 1) = q .+ Dp .* [
28     s1_itp(q[1], q[2]),
29     s2_itp(q[1], q[2])]

```

Listing 4: Zel'dovich Approximation for Caustics and Postions

```

1 function div_mod(f, grf::GRF)
2     k = sqrt.(grf.kx.^2 + grf.ky.^2)
3     a = convolve(k, f)
4     return a

```

```

5  end
6
7  function inv_div(f, grf::GRF)
8      k = sqrt.(grf.kx.^2 + grf.ky.^2)
9      P = grf.Pk
10     f_new = fft(f)
11     f_a = f_new .* k.^(-1)
12     f_a[1,1] = 0
13     a = real(ifft(f_a))
14     return a
15 end
16
17 function laplacian_inv(f, grf::GRF)
18     k = sqrt.(grf.kx.^2 + grf.ky.^2)
19     f_new = fft(f)
20     f_a = f_new .* k.^(-2)
21     f_a[1,1] = 0
22     a = real(ifft(f_a))
23     return a
24 end
25
26 function laplacian(f, grf::GRF)
27     k = sqrt.(grf.kx.^2 + grf.ky.^2)
28     a = convolve(k.^2,f)
29     return a
30 end
31
32 function equi_field(field,phi, f_NL)
33     equi1 = -3 .* field.^2 +
34             4 .* inv_div((field .* div_mod(field, phi)) , phi) +
35             2 .* laplacian_inv((field .* laplacian(field,phi)),
36             phi) +
37             2 .* laplacian_inv((div_mod(field,phi)).^2, phi)
38     new_field = field + f_NL .* equi1
39     return new_field
40 end
41
42 function orto_field(field,phi, f_NL)
43     equi1 = -9 .* field.^2 +
44             10 .* inv_div((field .* div_mod(field, phi)) , phi) +
45             8 .* laplacian_inv((field .* laplacian(field,phi)),
46             phi) +
47             8 .* laplacian_inv((div_mod(field,phi)).^2, phi)
48     new_field = field + f_NL .* equi1
49     return new_field
50 end
51
52 function local_field(field, f_NL)
53     field_local = field + f_NL * field.^2

```

```

52     return field_local
53 end

```

Listing 5: Non-Gaussianities Generating code

```

1 convolve(a, b) = real(ifft(conj.(a) .* fft(b)))
2
3 grad(f, cgrf::GRF) = stack([
4     convolve(im * cgrf.kx, f),
5     convolve(im * cgrf.ky, f)])
6
7 hessian(f, cgrf::GRF) = stack([
8     convolve(-cgrf.kx .* cgrf.kx, f),
9     convolve(-cgrf.kx .* cgrf.ky, f),
10    convolve(-cgrf.ky .* cgrf.ky, f)])
11
12 function directional_derivative_1(eig1_grad, v1, i, j, i_ref,
13     j_ref)
14     return sign(dot(v1[i_ref, j_ref, :], v1[i, j, :])) * dot(v1[i
15         , j, :], eig1_grad[i, j, :])
16 end

```

Listing 6: Auxiliary code

## D Further Non-Gaussian Realizations

Having studied the impacts of non-gaussianities on a field of length  $L=10$ , it is relevant to study how this fares for larger scales. In this section we present the evolution of the caustics of the first eigenvalue field for a field of length  $L=50$ . As it is possible to see, our main conclusions remain true, there are visible changes for all types of non-gaussianities from  $f_{NL} \approx 0.01$ , although for an higher resolution than the one in this report, there are visible changes from  $f_{NL} \approx 0.001$ .

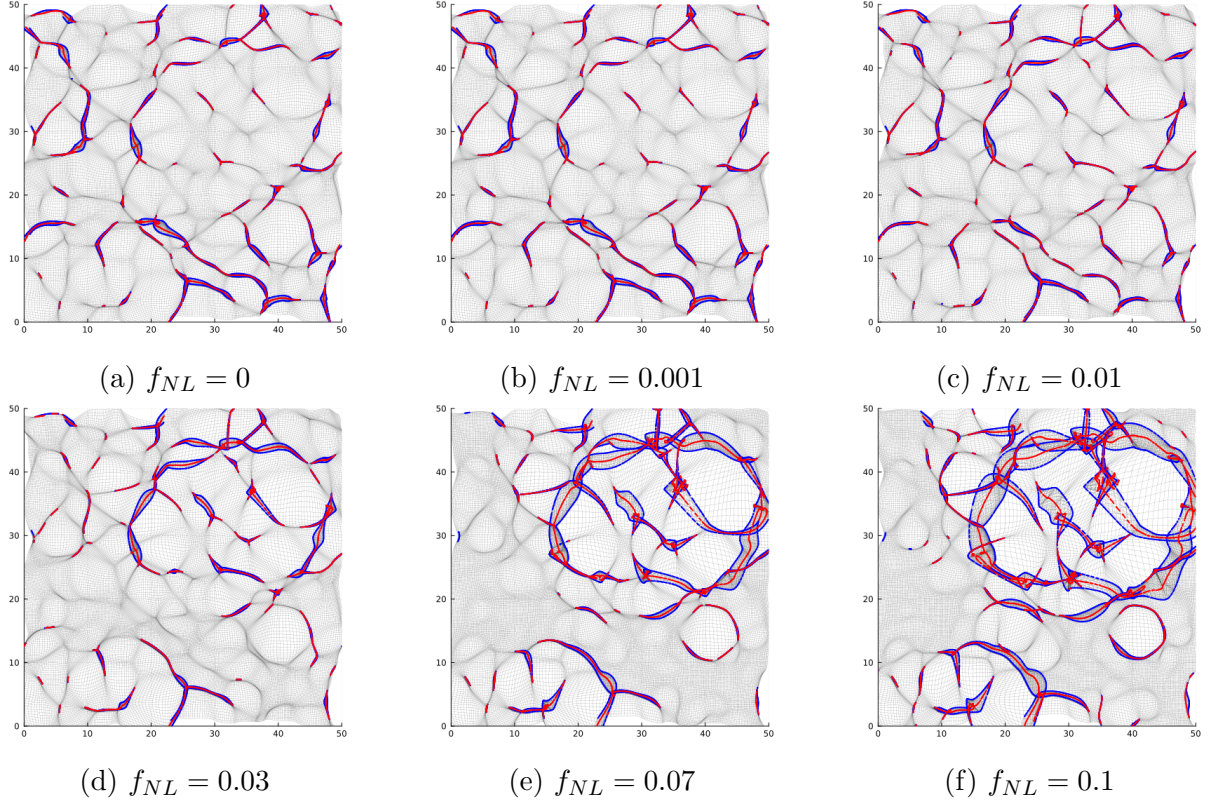


Figure 12: Local Non-gaussianities in Eulerian space

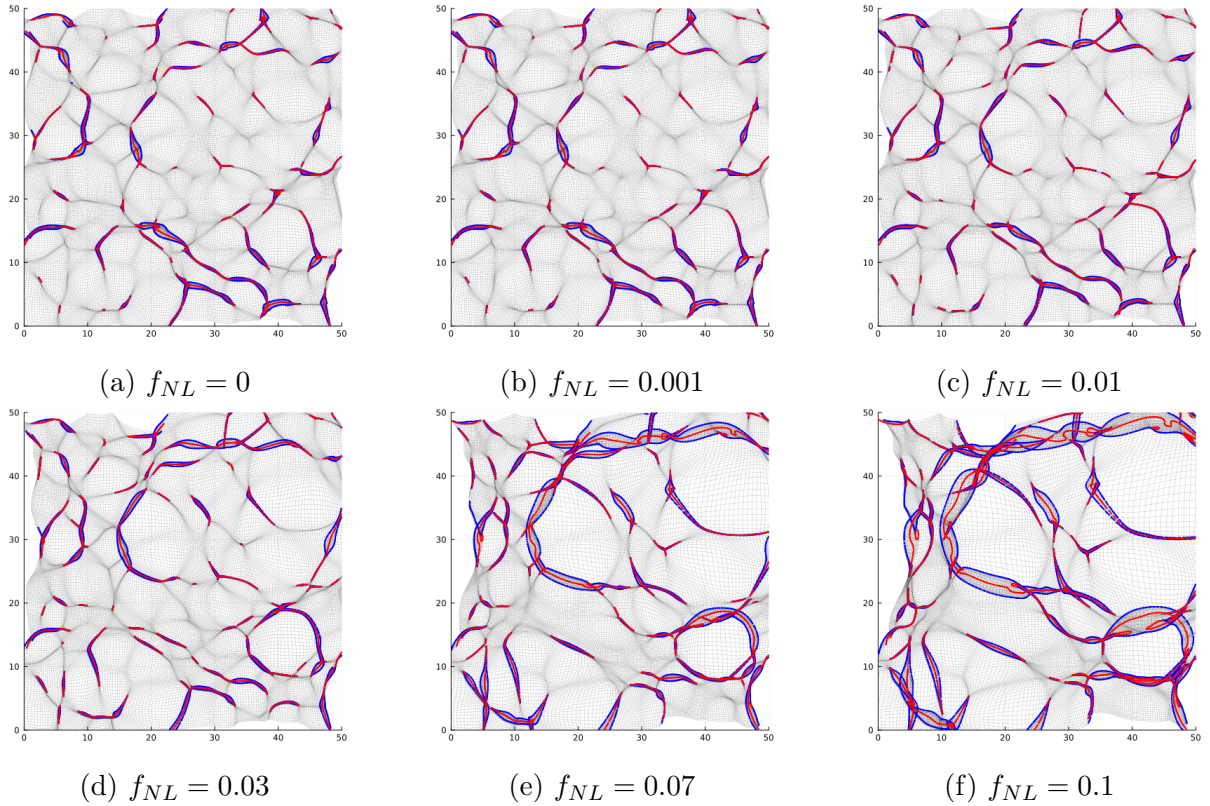


Figure 13: Equilateral Non-gaussianities in Eulerian space

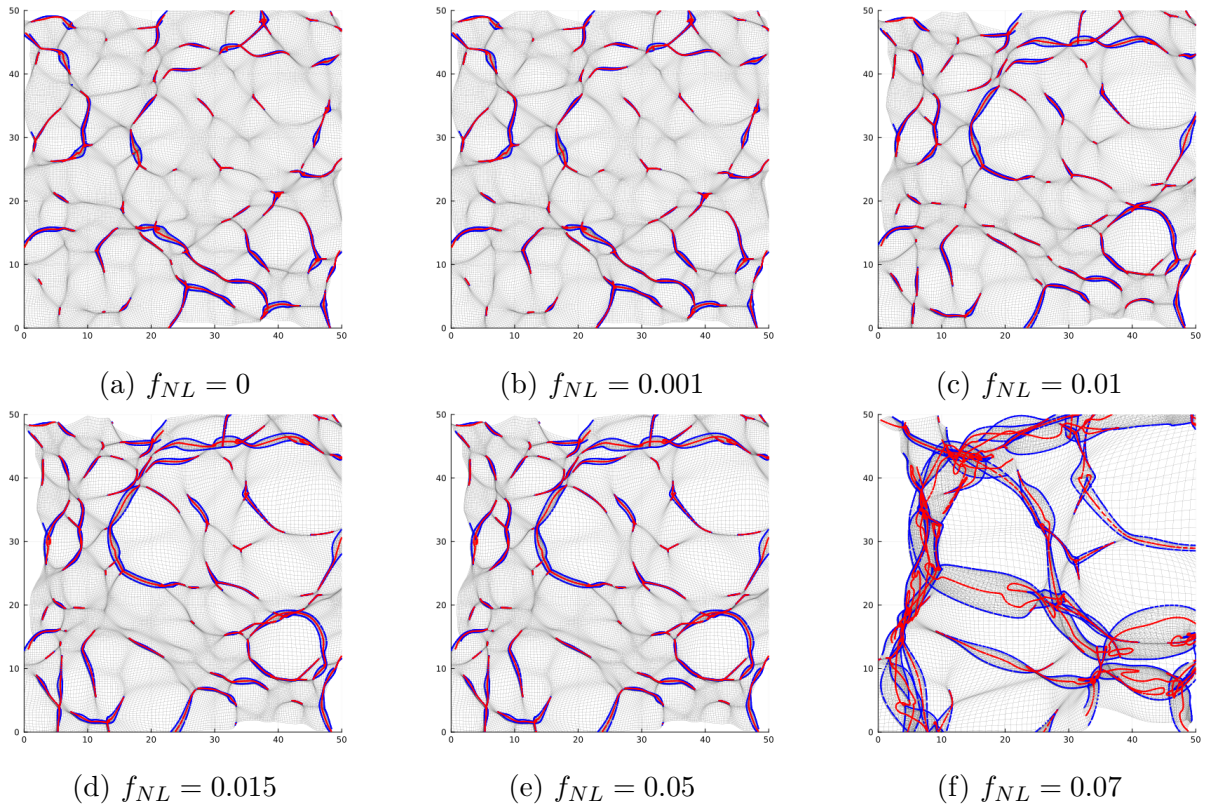


Figure 14: Orthogonal Non-gaussianities in Eulerian space